A Reemerging Bright Soft X-Ray State of the Changing-look Active Galactic Nucleus 1ES 1927+654

Ghosh, Ritesh; Laha, Sibasish; Meyer, Eileen; Roychowdhury, Agniva; Yang, Xiaolong; Acosta–Pulido, J. A.; Rakshit, Suvendu; Pandey, Shivangi; González, Josefa Becerra; Behar, Ehud; Gallo, Luigi C.; Panessa, Francesca; Bianchi, Stefano; La Franca, Fabio; Scepi, Nicolas; Begelman, Mitchell C.; Longinotti, Anna Lia; Lusso, Elisabeta; Oates, Samantha; Nicholl, Matt

DOI:
10.3847/1538-4357/aced92

Document Version
Publisher's PDF, also known as Version of record

Citation for published version (Harvard):
Ghosh, R, Laha, S, Meyer, E, Roychowdhury, A, Yang, X, Acosta–Pulido, JA, Rakshit, S, Pandey, S, González, JB, Behar, E, Gallo, LC, Panessa, F, Bianchi, S, La Franca, F, Scepi, N, Begelman, MC, Longinotti, AL, Lusso, E, Oates, S, Nicholl, M, Cenko, SB, O'Connor, B, Hammerstein, E, Jose, J, Gabányi, KÉ, Ricci, F & Chattopadhyay, S 2023, 'A Reemerging Bright Soft X-Ray State of the Changing-look Active Galactic Nucleus 1ES 1927+654: A Multiwavelength View', *The Astrophysical Journal*, vol. 955, no. 1, 3. https://doi.org/10.3847/1538-4357/aced92

The Astrophysical Journal, 955:3 (19pp), 2023 September 20 https://doi.org/10.3847/1538-4357/aced92

A Reemerging Bright Soft X-Ray State of the Changing-look Active Galactic Nucleus 1ES 1927+654: A Multiwavelength View

Ritesh Ghosh[1,2,3], Sibasish Laha[1,2,3], Eileen Meyer[4], Agniva Roychowdhury[4], Xiaolong Yang[5,6], J. A. Acosta–Pulido[7,8], Suvendu Rakshit[9], Shivangi Pandey[9], Josefa Becerra González[7,8], Ehud Behar[10], Luigi C. Gallo[11], Francesca Panessa[12], Stefano Bianchi[13], Fabio La Franca[13], Nicolas Scepi[14], Mitchell C. Begelman[15], Anna Lia Longinotti[16], Elisabeta Lusso[17,18], Samantha Oates[19], Matt Nicholl[20], S. Bradley Cenko[2,21], Brendan O'Connor[2,22,23,24], Erica Hammerstein[2,3,24], Jincen Jose[9], Krisztina Éva Gabányi[25,26,27], Federica Ricci[13,28], and Sabyasachi Chattopadhyay[29]

[1] Center for Space Science and Technology, University of Maryland Baltimore County, 1000 Hilltop Circle, Baltimore, MD 21250, USA; ritesh.ghosh@nasa.gov, ritesh.ghosh1987@gmail.com
[2] Astrophysics Science Division, NASA Goddard Space Flight Center, Greenbelt, MD 20771, USA
[3] Center for Research and Exploration in Space Science and Technology, NASA/GSFC, Greenbelt, MD 20771, USA
[4] Department of Physics, University of Maryland, Baltimore County, 1000 Hilltop Circle, Baltimore, MD 21250, USA
[5] Shanghai Astronomical Observatory, Chinese Academy of Sciences, Shanghai 200030, People's Republic of China
[6] Kavli Institute for Astronomy and Astrophysics, Peking University, Beijing 100871, People's Republic of China
[7] Instituto de Astrofísica de Canarias (IAC), E-38200 La Laguna, Tenerife, Spain
[8] Universidad de La Laguna (ULL), Departamento de Astrofísica, E-38206 La Laguna, Tenerife, Spain
[9] Aryabhatta Research Institute of Observational Sciences (ARIES), Manora Peak, Nainital, 263002 India
[10] Department of Physics, Technion, Haifa 32000, Israel
[11] Department of Astronomy & Physics, Saint Mary's University, 923 Robie Street, Halifax, Nova Scotia, B3H 3C3, Canada
[12] INAF—Istituto di Astrofisica e Planetologia Spaziali, via Fosso del Cavaliere 100, I-00133 Roma, Italy
[13] Dipartimento di Matematica e Fisica, Università degli Studi Roma Tre, Via della Vasca Navale 84, I-00146, Roma, Italy
[14] School of Physics and Astronomy, University of Southampton, Highfield, Southampton, SO17 1BJ, UK
[15] JILA, University of Colorado and National Institute of Standards and Technology, 440 UCB, Boulder, CO 80309-0440, USA
[16] Instituto de Astronomía, Universidad Nacional Autónoma de México, Circuito Exterior, Ciudad Universitaria, Ciudad de México 04510, México
[17] Dipartimento di Fisica e Astronomia, Università di Firenze, Via G. Sansone 1, I-50019, Sesto Fiorentino, Firenze, Italy
[18] INAF—Osservatorio Astrofisico di Arcetri, Largo Enrico Fermi 5, I-50125, Firenze, Italy
[19] Birmingham Institute for Gravitational Wave Astronomy and School of Physics and Astronomy, University of Birmingham, Birmingham, B15 2TT, UK
[20] Astrophysics Research Centre, School of Mathematics and Physics, Queens University Belfast, Belfast, BT7 1NN, UK
[21] Joint Space-Science Institute, University of Maryland, College Park, MD 20742, USA
[22] Department of Physics, The George Washington University, Washington, DC 20052, USA
[23] Astronomy, Physics and Statistics Institute of Sciences (APSIS), The George Washington University, Washington, DC 20052, USA
[24] Department of Astronomy, University of Maryland, College Park, MD 20742-4111, USA
[25] Department of Astronomy, Institute of Physics and Astronomy, ELTE Eötvös Loránd University, Pázmány Péter sétány 1/A, H-1117 Budapest, Hungary
[26] Konkoly Observatory, ELKH Research Centre for Astronomy and Earth Sciences, Konkoly Thege Miklós út 15-17, H-1121 Budapest, Hungary
[27] ELKH-ELTE Extragalactic Astrophysics Research Group, ELTE Eötvös Loránd University, Pázmány Péter sétány 1/A, H-1117 Budapest, Hungary
[28] INAF—Osservatorio Astronomico di Roma, via Frascati 33, 00040 Monteporzio Catone, Italy
[29] South African Astronomical Observatory, 1 Observatory Rd, Observatory, Cape Town, 7925, South Africa
Received 2023 May 18; revised 2023 July 22; accepted 2023 August 4; published 2023 September 11

Abstract

1ES1927+654 is a nearby active galactic nucleus (AGN) that has shown an enigmatic outburst in optical/UV followed by X-rays, exhibiting strange variability patterns at timescales of months to years. Here we report the unusual X-ray, UV, and radio variability of the source in its postflare state (2022 January–2023 May). First, we detect an increase in the soft X-ray (0.3–2 keV) flux from 2022 May to 2023 May by almost a factor of 5, which we call the bright soft state. The hard X-ray 2–10 keV flux increased by a factor of 2, while the UV flux density did not show any significant changes ($\leqslant$30%) in the same period. The integrated energy pumped into the soft and hard X-rays during this period of 11 months is $\sim 3.57 \times 10^{50}$ erg and 5.9×10^{49} erg, respectively. From the energetics, it is evident that whatever is producing the soft excess (SE) is pumping out more energy than either the UV or hard X-ray source. Since the energy source presumably is ultimately the accretion of matter onto the supermassive black hole, the SE-emitting region must be receiving the majority of this energy. In addition, the source does not follow the typical disk–corona relation found in AGNs, neither in the initial flare (from 2017 to 2019) nor in the current bright soft state (2022–2023). We found that the core ($<$1 pc) radio emission at 5 GHz gradually increased until 2022 March, but showed a dip in 2022 August. The Güdel–Benz relation ($L_{\rm radio}/L_{\rm X\text{-}ray} \sim 10^{-5}$), however, is still within the expected range for radio-quiet AGNs, and further follow-up radio observations are currently being undertaken.

Unified Astronomy Thesaurus concepts: Active galactic nuclei (16); X-ray active galactic nuclei (2035); Seyfert galaxies (1447)

1. Introduction

Active galactic nuclei (AGNs) are astrophysical systems hosting an accreting supermassive black hole (SMBH) and emitting across all wavelength bands through various physical processes. However, the exact physics of how matter from

larger distances (>1 pc) loses angular momentum and falls into the accretion disk of the SMBH, thereby creating enormous luminosity, is still not properly understood. Similarly, it is also not clear how the hot ($T \sim 10^9$ K) X-ray emitting plasma (corona), very commonly found in AGNs, is energetically supported by the accreting system. Ideally, one would understand the physics behind these emission features when they switch on and off or show extreme variability. However, our understanding of these systems is much hindered by their long duty cycle ($\sim 10^7$–10^9 yr; see, e.g., Marconi et al. 2004; Schawinski et al. 2015) compared to the human timescale, thus preventing us from detecting an ignition or quenching event.

However, recent large-scale time-domain surveys, e.g., the All-Sky Automated Survey for Supernovae (Shappee et al. 2014), the Zwicky Transient Facility (ZTF; Bellm et al. 2019), and others, have led to the identification of new types of extreme variability in active galaxies, called "changing-look" or "changing-state" AGNs (CL-AGNs). These extreme variations are characterized by order-of-magnitude changes in the optical, UV, and X-ray luminosity of the source, coupled with a rapid transition between spectral states (type 1 to type 2 and vice versa). For example, sources initially exhibiting AGN type-2 characteristics, with the optical/UV band dominated by narrow emission lines only, have transitioned to a type-1 state, displaying prominent broad emission lines and vice versa. There is often also a change in the optical continuum slope from red to blue, coinciding with the appearance/disappearance of broad lines (LaMassa et al. 2015; Ruan et al. 2019). We note here that there are two types of CL-AGNs, changing-obscuration AGNs and changing-accretion-state AGNs. The CL-AGNs we talk about in this work relate to the sources exhibiting rapid accretion state changes, and not obscuration changes (Ricci & Trakhtenbrot 2022).

1ES 1927+654 (alias AT2018zf, ASASSN-18el) is one such CL-AGN that has undergone some dramatic changes (Trakhtenbrot et al. 2019; Ricci et al. 2020, 2021; Laha et al. 2022; Li et al. 2022; Masterson et al. 2022) in the recent past, showing behavior unlike other known CL-AGNs. Previous optical and X-ray studies (Boller et al. 2003; Gallo et al. 2013) have shown that despite having only narrow emission lines in the optical spectrum, there is no evidence of the line-of-sight absorption in any wavelength, thus it exhibits a "true type-2" behavior, meaning that the broadline region is simply intrinsically absent or too weak to be detected for this source. In 2017 December, it showed a sudden rise in the optical/UV flux, by almost four magnitudes, which peaked around ∼200 days after the start of the burst. The other interesting events that followed in the next few months to years are; broad emission lines appeared in this "true type-2 AGN" after ∼200 days of the initial flare, which stayed on for another ∼300 days and then gradually vanished; the X-rays gradually dimmed after ∼3–4 months of the optical flare and the 2–10 keV hard X-rays completely vanished in 2018 August for almost three months (2018 August–2018 October); the hard X-rays revived after 2018 October and flared up to ∼10 times its preflare value and stayed there for about a year; and there was no correlation between the soft and the hard X-ray variability, nor between the X-rays and the UV during this flaring event. The switching off of the corona where the 2–10 keV hard X-ray flux was completely gone (Ricci et al. 2020, 2021) is particularly a peculiar phenomenon that was first witnessed in this source. In the meantime, after the initial flare, the UV flux monotonically dimmed with $t^{-0.91\pm0.04}$ (Laha et al. 2022), returning to a near-preflare value after ∼1200 days of the initial flare. The core (<1 pc) radio flux density at 5 GHz showed a minimum (a factor of 4 below the preflare value) at the time when the X-ray flux was low, and it gradually increased over the next 2 yr. Some studies of this phenomenon claimed it to be a tidal disruption event (TDE; Ricci et al. 2020, 2021; Masterson et al. 2022). However, there were already some concerns about this description, such as the optical emission lines one would expect for a TDE-like event not being present (Trakhtenbrot et al. 2019) and the X-rays not varying in the usual way a TDE should do, following a UV flare with a time lag (Ricci et al. 2020). We note that some TDEs emit X-rays, but do not show the same UV/X-ray evolution (see, e.g., ASASSN-15oi and AT2019azh; Gezari 2021). However, the vanishing and reemergence of the coronal emission of 1ES 1927+654 are uncommon in TDEs, in addition to a flatter ($t^{-0.91\pm0.04}$) UV light curve. This result is also supported by high-cadence data from the Transiting Exoplanet Survey Satellite survey of the source (Hinkle et al. 2023). The completely independent variations of the UV and the X-rays pointed to two or more different physical processes (possibly involving the magnetic field in the accretion disk) apart from the accretion, which contributed to the X-ray variations.

Our earlier study (Laha et al. 2022) encompassing the entire event (2017 December–2021 December) suggested that this could be a case of the magnetic pole inversion of the SMBH. In such a case, matter exhibiting the opposite magnetic polarity is advected to the accretion disk, which cancels the existing magnetic field, therefore temporarily switching off the corona, which is dependent on the magnetic field. Further advection of matter with the opposite polarity builds up a strong magnetic field (now with reversed poles), which recreates the corona. Finally, the accretion rate gets back to the preflare value, and so does the X-ray emission (Scepi et al. 2021; Laha et al. 2022).

Other CL-AGNs, such as Mrk 590 (Denney et al. 2014; Mathur et al. 2018; Ghosh et al. 2022), Mrk 1080 (McElroy et al. 2016; Noda & Done 2018), and NGC 1566 (Parker et al. 2019; Tripathi & Dewangan 2022), have also shown different patterns of optical, UV, and X-ray variability and different timescales, mostly over several years. However, as it stands, the CL phenomenon in 1ES 1927+654 is one of the fastest detected so far, with the changes happening within just a few months. The study of these interesting sources not only helps us to understand how the accretion disk and the corona get coupled (with strong correlation between UV and X-rays) and decoupled (with no correlation) at different phases of evolution, but also how the soft X-ray emission in an AGN (popularly known as the soft X-ray excess, or SE) evolves with the other components of the central engine, which is an ideal technique for understanding its origin in the first place. Thus, these sources give us a unique view of how the soft and hard X-ray and UV evolve with time, the origin of the SE, and the relations between the emission in the different energy bands as they vary (e.g., radio and X-rays).

We have followed up 1ES 1927+654 with multiwavelength observations from space-based and ground-based missions to track its behavior in the postflare state. In this paper, we report another interesting phenomenon currently ongoing in the source, using multiwavelength data from Swift (X-ray and UV), the Himalayan Chandra Telescope (HCT; optical), the Lowell Discovery Telescope (LDT; optical), and the Very Long

Baseline Array (VLBA; radio). The paper is arranged as follows: Section 2 discusses the observation, data reduction, and analysis. Section 3 lists the most important results. Section 4 discusses the results and Section 5 lists the main conclusions. Throughout this paper, we assumed a cosmology with $H_0 = 71$ km s^{-1} Mpc^{-1}, $\Omega_\Lambda = 0.73$, and $\Omega_M = 0.27$. We regard a correlation to be significant if the confidence level is >99.99%.

2. Observations, Data Reduction, and Data Analysis

2.1. Swift X-Ray Telescope and UVOT

Observations of 1ES 1927+654 were carried out by the Neil Gehrels Swift Observatory (Swift) initially at a monthly cadence, from 2022 January to 2022 November, and then at a weekly and biweekly cadence, from 2022 December to 2023 May (See Table 1), under a Director's Discretionary Time (DDT) program (P.I.: S. Laha). The earlier Swift X-Ray Telescope (XRT; Burrows et al. 2005) and UVOT (Roming et al. 2005) observations of this source (prior to 2021 December 31) have been reported in our previous work (Laha et al. 2022), and we use those results in this work for comparison and to portray a complete picture of the phenomenon.

We followed the automated XRT analysis approach via the online tools[30] (Evans et al. 2009) for the XRT data in all our observations (S33–S78), as recommended for point sources (PSs) by the Swift help desk. Refer to Laha et al. (2022) for a full description of the UVOT data reprocessing and analysis, which we follow here. The UV flux densities were corrected for Galactic absorption using the correction magnitude of $A_\lambda = 0.690$ obtained from the NASA Extragalactic Database (NED).[31]

We used a simple absorbed power-law model in XSPEC (Arnaud 1996) to fit the 0.3–10 keV XRT grouped spectra (a minimum of 10 counts per bin) for all the Swift observations, and we added a blackbody component to model the SE below 2 keV. We note that adding a `blackbody` in the soft X-ray did not improve the fit statistics from observations S33 to S48. However, in the latest observations (S49–S78), where the soft X-ray flux increased notably, a `blackbody` component improved the fit statistics significantly, with a typical temperature $kT_e \sim 0.2$ keV. Table 2 quotes the best-fit parameters and fit statistics.

We measured the UV monochromatic flux using the UVW2 filter for all Swift observations and corrected it for Galactic reddening and extinction. We created the UVOT source and background spectral files using the UVOT2PHA tool and used the response files provided by the Swift team.

We estimated the bolometric luminosity ($L_{\rm bol}$) and hence the accretion rate ($\lambda_{\rm Edd}$) of the source using the relation $\lambda_{\rm Edd} = L_{\rm bol}/L_{\rm Edd}$, where $L_{\rm Edd}$ is the Eddington rate of the source, assuming a BH of mass $\sim 10^6 M_\odot$ (Ricci et al. 2020). The value is estimated using the galaxy's stellar mass, inferred from the K-band photometry relation from Kormendy & Ho (2013). Here, we note that the estimates of the BH mass of 1ES1927+654 varied up to $\sim 10^7 M_\odot$ (Trakhtenbrot et al. 2019), where the authors used the virial method of broad Balmer emission lines. However, it is possible that due to the transient nature of the event, the clouds emitting the broad Balmer lines might not have had the time to virialize, as shown by their variable widths (Ricci et al. 2020). To estimate $L_{\rm bol}$, we have used the simple approach $L_{\rm bol} = L_{\rm UV} + L_{\rm X\text{-}ray}$, where $L_{\rm UV}$ is the integrated UV luminosity in the band 0.001–100 eV obtained by fitting the Swift-UVOT photometric data, and $L_{\rm X-ray}$ is the X-ray luminosity in the band 0.3–10 keV measured from the best-fit model obtained from the spectral fitting of each observation. The UVOT data (the three UV monochromatic data points: UVM1, UVW1, and UVW2) for every Swift observation (S01–S78) have been fitted with a disk blackbody (diskbb) in XSPEC. The model in XSPEC reads as tbabs × REDDEN × diskbb, and the corresponding luminosity $L_{\rm UV}$ is measured using the command clumin, over the energy range 0.01–100 eV.

2.2. VLBA

1ES 1927+654 was observed by the VLBA on 2022 March 5 under DDT proposal BM527 (P.I.: E. Meyer) and as part of project BY177B (P.I.: X. Yang) on 2022 August 5. A standard dual-polarization 6 cm frequency setup was used, with central channel frequencies of 4868 MHz, 4900 MHz, 4932 MHz, 4964 MHz, 4996 MHz, 5028 MHz, 5060 MHz, and 5092 MHz, and a total bandwidth of 32 MHz. As the source was expected to be too faint for self-calibration, a relatively fast-switching cadence between the target and a bright calibrator source was used in both projects for phase referencing (Beasley & Conway 1995). The observations were 3.5 and 2.8 hr, resulting in acceptable *uv* coverage for imaging.

The data were checked for radio frequency interference and then calibrated using VLBARUN (the Astronomical Image Processing System VLBA pipeline; Greisen 1990). The imaging and analysis of source structure were done using a custom version of `DIFMAP` (Shepherd et al. 1994): `ngDIFMAP` (Roychowdhury et al. 2023). The best model (as discussed in Laha et al. 2022 for a previous VLBA observation), as determined by the reduced chi-squared value, is a PS centered on a uniformly bright disk. The details of the procedure are as given in Laha et al. (2022), and Table 3 lists the details of the PS and extended disk that were found to describe the source best. We used Monte Carlo simulations (e.g., Briggs 1995; Chael et al. 2018; Roychowdhury et al. 2023) to verify that the extended emission around the PS is intrinsic to the source and is not an artifact of interferometric errors. In Table 4, we list the ratio of the core radio flux density to the 2–10 keV flux (also known as the Güdel–Benz, or GB, relation; Güdel & Benz 1993).

We find that the PS flux density has increased by a factor of ∼1.8 in the year from 2021 March to 2022 March, followed by a decrease by a similar factor by 2022 August. The flux density of the uniform disk has remained mostly unchanged, while its structure has shrunk by ∼20% between 2021 March and 2022 August.

2.3. Optical Spectroscopy

2.3.1. The HCT Observation

We observed the source on 2022 October 31 using the 2 m HCT located at Hanle, India. We used grism 7, covering a wavelength range of 4000 Å to 7000 Å, and a 2″ slit for the observation. Flux calibration was done using a spectroscopic standard star, BD+28 4211. Standard spectroscopic reduction, using the IRAF package, is used to extract the spectra, including flat subtraction, wavelength, and flux calibration.

[30] https://www.swift.ac.uk/user-objects
[31] https://ned.ipac.caltech.edu

Table 1
The Details of the Multiwavelength Observations of 1ES 1927+654 Used in This Work

Observation Band	Telescope	Observation Date YYYY-MM-DD	Observation ID	Net Exposure (Sec)	Short ID
X-ray and UV	XMM-Newton EPIC-pn/OM	2011-05-20	0671860201	28,649	X1
”	Swift-XRT/UVOT	2018-05-17	00010682001	2190	S01
”	”	2022-03-22	00010682033	2056	S33
”	”	2022-04-23	00010682034	1276	S34
”	”	2022-05-20	00010682035	563	S35
”	”	2022-05-26	00010682036	884	S36
”	”	2022-06-20	00010682037	1469	S37
”	”	2022-07-20	00010682038	1412	S38
”	”	2022-08-20	00010682039	652	S39
”	”	2022-08-24	00010682040	1234	S40
”	”	2022-08-26	00010682041	1810	S41
”	”	2022-09-26	00010682042	2166	S42
”	”	2022-10-28	00010682043	411	S43
”	”	2022-11-20	00010682044	797	S44
”	”	2022-11-26	00010682045	1768	S45
”	”	2022-12-03	00010682046	988	S46
”	”	2022-12-14	00010682047	3001	S47
”	”	2022-12-17	00010682048	1441	S48
”	”	2022-12-21	00010682049	1989	S49
”	”	2023-01-03	00010682050	712	S50
”	”	2023-01-07	00010682051	860	S51
”	”	2023-01-14	00010682052	2958	S52
”	”	2023-01-21	00010682053	817	S53
”	”	2023-01-25	00010682054	1907	S54
”	”	2023-01-28	00010682055	1926	S55
”	”	2023-02-01	00010682056	1712	S56
”	”	2023-02-04	00010682057	922	S57
”	”	2023-02-08	00010682058	1883	S58
”	”	2023-02-11	00010682059	974	S59
”	”	2023-02-13	00010682060	1788	S60
”	”	2023-02-25	00010682061	842	S61
”	”	2023-02-27	00010682062	910	S62
”	”	2023-03-02	00010682063	1780	S63
”	”	2023-03-04	00010682064	891	S64
”	”	2023-03-08	00010682065	1800	S65
”	”	2023-03-11	00010682066	872	S66
”	”	2023-03-14	00010682067	868	S67
”	”	2023-03-18	00010682068	935	S68
”	”	2023-03-20	00010682069	1065	S69
”	”	2023-03-29	00010682071	809	S71
”	”	2023-03-30	00010682072	1066	S72
”	”	2023-04-16	00010682073	888	S73
”	”	2023-04-22	00010682074	938	S74
”	”	2023-04-29	00010682076	903	S76
”	”	2023-05-01	00010682077	1168	S77
”	”	2023-05-05	00010682078	902	S78
Optical	HTC	2022-10-31	HCT-2022-C3-P10	2400	
Radio	VLBA	2022-03-05	BM527	12,600	
”	VLBA	2022-08-05	BY177B	10,080	

Note. Refer to Laha et al. (2022) for all the previous Swift observations. The XMM-Newton observation is used as a comparison for the preflare X-ray state.

To estimate the spectral properties of the optical emission line, we first modeled the host galaxy using the PPXF code (Cappellari 2017) and MILES stellar templates (Falcón-Barroso et al. 2011). We subtracted the best-fit stellar model from the spectrum, leading to the pure AGN spectrum. Prominent narrow emission lines, such as [O III], N II, and [S II], are clearly present in the optical spectrum; however, the Hβ line is only detected in the host-subtracted spectrum. This is similar to our earlier findings in Laha et al. (2022). To estimate the emission-line flux and width, we performed a multi-component modeling of the host-subtracted spectrum, using Gaussian functions separately for the Hβ and Hα regions. We model all the narrow components using a single Gaussian. In the Hβ complex, narrow Hβ and the [O III]4959, 5007 doublets were modeled, while keeping the flux ratio fixed at theoretical values. In the Hα region, the narrow Hα, [N II]6549, [N II]

Table 2
The Spectral Parameters Obtained Using Swift and XMM-Newton UV and X-Ray Observations of 1ES 1927+654

ID (DD/MM/YY)	$F_{0.3-2\ \mathrm{keV}}$[a]	$F_{2-10\ \mathrm{keV}}$[a]	$F_{1.5-2.5\ \mathrm{keV}}$[a]	kT (keV)	Γ	UV Filter	UV Flux Density[b]	α_{OX}	χ^2/χ^2_ν
X1 (20/05/11)	9.41 ± 0.66	3.92 ± 0.08	1.64 ± 0.02	0.20 ± 0.01	$2.21^{+0.02}_{-0.02}$	UVM2	1.34 ± 0.03	1.004	185/1.37
S33 (22/03/22)	18.26 ± 1.34	4.66 ± 0.66	2.49 ± 0.22	⋯	$2.67^{+0.10}_{-0.09}$	UVW2	2.00 ± 0.09	1.002	119.36/1.03
S34 (23/04/22)	14.46 ± 1.40	4.59 ± 0.66	2.25 ± 0.20	⋯	$2.55^{+0.14}_{-0.14}$	UVW2	2.04 ± 0.09	1.022	75.91/0.90
S35 (20/05/22)	8.70 ± 1.71	2.81 ± 1.05	1.37 ± 0.30	⋯	$2.54^{+0.27}_{-0.24}$	UVW2	1.83 ± 0.08	1.087	27.03/1.13
S36 (26/05/22)	10.04 ± 1.48	5.02 ± 1.79	2.12 ± 0.36	⋯	$2.26^{+0.22}_{-0.22}$	UVW2	1.91 ± 0.12	1.021	34.49/0.84
S37 (20/06/22)	12.42 ± 1.30	4.03 ± 0.89	1.96 ± 0.26	⋯	$2.54^{+0.15}_{-0.14}$	UVW2	1.91 ± 0.09	1.034	47.19/0.73
S38 (20/07/22)	13.66 ± 1.46	5.22 ± 1.04	2.37 ± 0.29	⋯	$2.45^{+0.14}_{-0.13}$	UVW2	2.04 ± 0.09	1.013	68.35/1.04
S39 (20/08/22)	18.23 ± 2.03	6.35 ± 1.37	2.99 ± 0.39	⋯	$2.50^{+0.15}_{-0.14}$	UVW2	2.28 ± 0.13	0.993	35.88/0.61
S40 (24/08/22)	20.39 ± 2.16	5.37 ± 1.16	2.83 ± 0.37	⋯	$2.66^{+0.15}_{-0.14}$	UVW2	2.02 ± 0.09	0.982	59.22/0.90
S41 (26/08/22)	14.14 ± 1.16	4.62 ± 0.76	2.24 ± 0.22	⋯	$2.54^{+0.11}_{-0.11}$	UVW2	2.24 ± 0.11	1.038	99.27/0.97
S42 (26/09/22)	17.71 ± 1.23	4.79 ± 0.67	2.50 ± 0.21	⋯	$2.64^{+0.09}_{-0.09}$	UVW2	1.98 ± 0.09	0.999	115.91/0.92
S43 (28/10/22)	19.71 ± 3.08	6.55 ± 2.22	3.15 ± 0.62	⋯	$2.52^{+0.23}_{-0.22}$	UVW2	1.96 ± 0.10	0.959	45.61/1.26
S44 (20/11/22)	25.55 ± 4.95	6.35 ± 2.42	3.43 ± 0.79	⋯	$2.69^{+0.24}_{-0.24}$	UVW2	2.02 ± 0.12	0.950	33.98/0.85
S45 (26/11/22)	26.02 ± 2.17	7.18 ± 1.15	3.72 ± 0.37	⋯	$2.73^{+0.11}_{-0.10}$	UVW2	2.30 ± 0.13	0.958	78.79/0.89
S46 (03/12/22)	42.71 ± 5.76	10.52 ± 3.24	5.70 ± 1.03	⋯	$2.69^{+0.21}_{-0.20}$	UVW2	2.00 ± 0.09	0.864	28.10/0.62
S47 (14/12/22)	26.01 ± 1.51	6.14 ± 0.71	3.38 ± 0.25	⋯	$2.71^{+0.08}_{-0.07}$	UVW2	2.02 ± 0.11	0.952	161.52/1.11
S48 (17/12/22)	25.92 ± 1.72	5.41 ± 0.70	3.14 ± 0.27	⋯	$2.79^{+0.09}_{-0.09}$	UVW2	1.86 ± 0.10	0.951	89.07/0.70
S49 (21/12/22)	34.81 ± 2.12	10.12 ± 1.84	5.10 ± 0.44	0.20 ± 0.05	$2.47^{+0.16}_{-0.19}$	UVW2	2.00 ± 0.10	0.882	126.62/0.86
S50 (02/01/23)	27.22 ± 3.05	11.54 ± 4.85	3.68 ± 0.78	0.17 ± 0.04	$2.01^{+0.50}_{-0.90}$	UVW2	1.76 ± 0.10	0.915	23.36/0.83
S51 (07/01/23)	39.74 ± 3.94	8.01 ± 2.49	4.31 ± 0.65	0.17 ± 0.04	$2.56^{+0.29}_{-0.41}$	UVW2	1.87 ± 0.11	0.899	66.94/0.96
S52 (14/01/23)	32.95 ± 1.68	6.42 ± 1.06	3.80 ± 0.27	0.19 ± 0.03	$2.67^{+0.14}_{-0.16}$	UVW2	1.91 ± 0.11	0.924	151.81/0.95
S53 (21/01/23)	30.75 ± 2.83	7.41 ± 2.47	3.70 ± 0.49	0.19 ± 0.03	$2.29^{+0.33}_{-0.49}$	UVW2	1.96 ± 0.11	0.932	74.32/1.08
S54 (25/01/23)	37.19 ± 2.26	7.89 ± 1.51	4.82 ± 0.46	0.22 ± 0.05	$2.64^{+0.16}_{-0.17}$	UVW2	1.89 ± 0.11	0.882	112.22/0.80
S55 (28/01/23)	42.53 ± 2.80	8.30 ± 1.79	5.19 ± 0.50	0.20 ± 0.02	$2.54^{+0.19}_{-0.22}$	UVW2	1.63 ± 0.22	0.845	119.84/0.92
S56 (01/02/23)	34.86 ± 2.24	6.12 ± 0.99	3.54 ± 0.24	0.19 ± 0.03	$2.54^{+0.27}_{-0.22}$	UVW2	1.96 ± 0.11	0.940	106.9/0.86
S57 (04/02/23)	35.95 ± 3.20	6.22 ± 2.19	3.86 ± 0.51	0.19 ± 0.05	$2.68^{+0.30}_{-0.39}$	UVW2	1.91 ± 0.11	0.921	74.79/0.95
S58 (08/02/23)	35.74 ± 1.98	8.82 ± 1.39	4.11 ± 0.31	0.17 ± 0.02	$2.36^{+0.21}_{-0.26}$	UVW2	1.62 ± 0.11	0.883	134.25/0.91
S59 (11/02/23)	38.15 ± 3.56	6.54 ± 1.82	3.59 ± 0.51	0.15 ± 0.03	$2.66^{+0.27}_{-0.36}$	UVW2	1.60 ± 0.08	0.904	66.18/0.89
S60 (13/02/23)	31.94 ± 2.09	7.71 ± 3.20	3.78 ± 0.35	0.16 ± 0.03	$2.48^{+0.20}_{-0.24}$	UVW2	2.02 ± 0.13	0.934	92.94/0.74
S61 (25/02/23)	37.50 ± 4.15	6.83 ± 2.44	5.14 ± 1.08	0.25 ± 0.06	$2.96^{+0.36}_{-0.37}$	UVW2	2.17 ± 0.15	0.895	58.62/0.95
S62 (27/02/23)	42.61 ± 3.56	7.18 ± 2.31	4.35 ± 0.53	0.19 ± 0.03	$2.55^{+0.38}_{-0.36}$	UVW2	1.76 ± 0.10	0.887	71.96/0.83
S63 (02/03/23)	38.06 ± 2.43	8.31 ± 1.85	4.08 ± 0.37	0.18 ± 0.02	$2.34^{+0.26}_{-0.28}$	UVW2	1.89 ± 0.11	0.910	146.87/1.15
S64 (04/03/23)	44.42 ± 3.53	8.40 ± 2.15	5.33 ± 0.68	0.21 ± 0.05	$2.63^{+0.24}_{-0.24}$	UVW2	1.81 ± 0.11	0.858	65.41/0.71
S65 (08/03/23)	33.07 ± 2.03	6.60 ± 1.36	3.43 ± 0.31	0.17 ± 0.02	$2.51^{+0.23}_{-0.29}$	UVW2	1.91 ± 0.11	0.941	122.24/0.91
S66 (11/03/23)	42.65 ± 4.15	10.90 ± 3.15	4.88 ± 0.63	0.17 ± 0.03	$2.27^{+0.40}_{-0.30}$	UVW2	1.67 ± 0.10	0.860	61.13/0.90
S67 (14/03/23)	39.96 ± 3.76	9.35 ± 3.11	4.96 ± 0.65	0.19 ± 0.05	$2.52^{+0.31}_{-0.40}$	UVW2	1.83 ± 0.11	0.872	58.54/0.81
S68 (18/03/23)	41.08 ± 3.53	8.52 ± 2.64	4.28 ± 0.53	0.18 ± 0.02	$2.27^{+0.37}_{-0.53}$	UVW2	2.02 ± 0.11	0.913	71.32/0.91
S69 (20/03/23)	43.01 ± 5.17	9.53 ± 2.97	5.71 ± 0.98	0.24 ± 0.06	$2.70^{+0.43}_{-0.44}$	UVW2	1.54 ± 0.09	0.820	56.39/1.01
S71 (29/03/23)	36.97 ± 3.29	9.87 ± 2.95	4.31 ± 0.55	0.17 ± 0.02	$2.27^{+0.32}_{-0.43}$	UVW2	2.18 ± 0.12	0.925	82.06/1.05
S72 (30/03/23)	39.48 ± 3.27	4.49 ± 1.67	2.86 ± 0.42	0.17 ± 0.02	$2.69^{+0.36}_{-0.55}$	UVW2	2.33 ± 0.15	1.004	69.94/0.82
S73 (16/04/23)	36.48 ± 2.89	7.00 ± 1.93	4.10 ± 0.45	0.19 ± 0.05	$2.63^{+0.26}_{-0.31}$	UVW2	1.80 ± 0.09	0.901	86.08/0.90
S74 (22/04/23)	42.50 ± 3.93	7.95 ± 3.00	4.80 ± 0.65	0.20 ± 0.04	$2.63^{+0.32}_{-0.49}$	UVW2	2.28 ± 0.12	0.914	66.04/0.85
S76 (29/04/23)	46.08 ± 6.15	9.00 ± 4.87	4.60 ± 0.97	0.18 ± 0.04	$2.30^{+0.66}_{-0.69}$	UVW2	2.28 ± 0.13	0.921	33.75/0.87
S77 (01/05/23)	40.69 ± 3.55	4.32 ± 1.44	3.29 ± 0.44	0.19 ± 0.03	$2.90^{+0.29}_{-0.34}$	UVW2	2.09 ± 0.09	0.963	83.03/1.00
S78 (05/05/23)	41.17 ± 3.68	7.07 ± 2.41	4.44 ± 0.59	0.20 ± 0.04	$2.58^{+0.32}_{-0.47}$	UVW2	2.11 ± 0.11	0.914	40.89/0.62

Notes. For comparison with the preflare values, we keep the XMM-Newton observation.
[a] Flux in units of 10^{-12} erg cm^{-2} s^{-1} corrected for Galactic absorption.
[b] UV flux density in units of 10^{-15} erg cm^{-2} s^{-1}Å^{-1} $\alpha_{\mathrm{OX}} = -0.385 \log(F_{2\ \mathrm{keV}}/F_{2500\text{Å}})$. The UV flux density was corrected for Galactic absorption using the correction magnitude of $A_\lambda = 0.690$ obtained from NED.

6568, [S II]6717, and [S II]6732 were modeled, where the flux ratio of the N II doublets was fixed to their theoretical values, and the flux ratio of the S II doublets was fixed to unity. During the fit, the velocity shift and width were kept as free parameters. The best-fit model was obtained via the chi-square minimization method, and the uncertainty on the model parameter was obtained by the Monte Carlo approach (see Rakshit et al. 2020). We noticed excess emission in the residual spectrum around the Hα line while modeling with a single Gaussian (narrow component). Therefore, we have added another Gaussian profile with a line FWHM larger than 900 km s^{-1} to represent the broad component for Hα regions. We find a statistically improved fit with this addition of the broad component. Please see Table 5 for details.

Table 3
Details of the Radio Observations, with Corresponding Flux Density Measurements

Obs.	Freq. (GHz)	Date (MM/YY)	Total Flux (mJy beam^{-1})	Central PS Flux (mJy)	Extended Flux (mJy)	Disk Dimensions (mas × mas)	rms (Jy beam^{-1})	Resolution (mas × mas)	T_B ($\times 10^6$ K)
VLBA	4.98	03/22	6.6 ± 0.5	2.4 ± 0.1	4.2 ± 0.4	$4.4 \pm 0.1 \times 4.2 \pm 0.1$	1.0×10^{-4}	3.42×1.72	>9.7
VLBA	4.98	08/22	5.6 ± 0.5	1.5 ± 0.1	4.1 ± 0.4	$4.0 \pm 0.1 \times 3.2 \pm 0.1$	6.8×10^{-5}	3.59×1.36	>5.7

Note. In cases where only an unresolved core is observed, the total flux density equals the core flux density. For cases where we detect resolved extended emission, the central PS flux density is noted alongside the extended flux density and the semimajor and semiminor axes of a best-fitting uniform disk model. Note that "flux" in the table headings refers to flux density. The brightness temperature T_B (lower limit; Kovalev et al. 2005) has been calculated for the PS at 5 GHz.

Table 4
Semicontemporaneous X-Ray and Radio Fluxes (Either from 1.5 or 5 GHz VLBI) and the GB Relation

X-Ray Epoch (MM/YY)	Mean 2–10 keV X-Ray Flux (F_X) (erg cm^{-2} s^{-1})	VLBI Epoch (MM/YY)	VLBI Flux (F_R) (erg cm^{-2} s^{-1})	Ratio of Mean Fluxes F_R/F_X
[a]05/11	$3.70 \pm 0.07 \times 10^{-12}$	08/13	$5.00 \pm 0.50 \times 10^{-16}$	$1.35 \pm 0.11 \times 10^{-4}$
[a]05/11	$3.70 \pm 0.07 \times 10^{-12}$	03/14	$1.80 \pm 0.20 \times 10^{-16}$	$4.86 \pm 0.05 \times 10^{-5}$
12/18	$1.70 \pm 0.50 \times 10^{-12}$	12/18	$3.50 \pm 0.30 \times 10^{-17}$	$2.05 \pm 0.42 \times 10^{-5}$
03/21	$4.40 \pm 1.04 \times 10^{-12}$	03/21	$6.40 \pm 0.50 \times 10^{-17}$	$1.45 \pm 0.23 \times 10^{-5}$
03/22	$4.66 \pm 0.66 \times 10^{-12}$	03/22	$1.10 \pm 0.05 \times 10^{-16}$	$2.36 \pm 0.07 \times 10^{-5}$
08/22	$5.80 \pm 0.90 \times 10^{-12}$	08/22	$6.40 \pm 0.50 \times 10^{-17}$	$1.10 \pm 0.09 \times 10^{-5}$

Note.
[a] There are no contemporary X-ray observations of this source along with VLBI in 2013 and 2014. Hence, we have used the 2–10 keV flux from the 2011 XMM-Newton observation.

2.3.2. The LDT Observation

We obtained optical spectroscopy on 2022 October 30 using the DeVeny spectrograph mounted on the 4.3 m LDT in Happy Jack, AZ, for a total exposure of 600 s. DeVeny was configured with the 300 g mm^{-1} grating and a 1.″5 slit width. The spectrum covers wavelengths of 3600–8000 Å at a dispersion of 2.2 Å pix^{-1}. The data were processed using the methods described in Prochaska et al. (2020); that is, performing bias subtraction, flat-fielding, cosmic-ray removal, trace extraction, and telluric corrections, with Ne, Ar, Hg, and Cd arc lamps being used for wavelength calibration. The spectrum was flux-calibrated using observations of the spectrophotometric standard star G191-B2B obtained on the same night.

The LDT spectrum does not have a good absolute flux calibration; hence, the spectrum was rescaled to have the same level as the Gran Telescopio CANARIAS (GTC) spectra in 2021, as indicated by the photometry obtained by ZTF (minimal change <0.03 magnitude). That is, the r and g magnitudes did not vary by more than 3%. First, the spectrum was corrected of galactic interstellar extinction. The stellar population contribution was subtracted using PPXF. The line measurements from the LDT observation are reported in Table 6 and are consistent with the results of HCT.

Table 5
Optical Emission-line Properties without the Broad Component (the Values with Broad Components are Given in Parentheses)

Line	Center Wavelength (Å)	FWHM (km s^{-1})	Flux (erg s^{-1} cm^{-2}) $\times 10^{-15}$
Hβ(NC)	4857.5 ± 3.9	899 ± 100	3.67 ± 0.30
[O III]4959	4953.6 ± 3.9	706 ± 71	3.78 ± 0.10
[O III]5007	5001.4 ± 3.9	721 ± 23	11.42 ± 0.30
[N II]6549	6548.5 ± 4.1	421 ± 63	0.72 ± 0.09
	(6551.17 ± 4.14)	(673 ± 170)	(0.50 ± 0.18)
Hα(BC)	(6563.5 ± 5.5)	(1172 ± 327)	(5.06 ± 1.30)
Hα(NC)	6564.0 ± 4.1	673 ± 63	5.94 ± 0.42
	(6564.8 ± 4.1)	(389 ± 66)	(1.98 ± 0.91)
[N II]6585	6585.5 ± 4.1	640 ± 106	2.23 ± 0.30
	(6587 ± 4.1)	(491 ± 149)	(1.48 ± 0.53)
[S II]6718	6718.1 ± 4.1	478 ± 113	0.68 ± 0.08
[S II]6732	6727.8 ± 4.1	520 ± 133	0.69 ± 0.09

3. Results

In our earlier work (Laha et al. 2022), we reported the "initial flare" (2018 May–2021 December) of the source 1ES 1927 +654. Here, we report the results from our continuing multiwavelength campaign from 2022 January to 2023 March. We detect a significant rise in the soft X-ray flux (by a factor of 5 in a matter of ∼11 months), which we call the bright soft state. Figure 1 shows the time evolution of the fluxes in 0.3–2 keV and 2–10 keV, the UVW2 flux density, and the core radio flux. In Figure 2, we have zoomed in to the time period when the soft X-ray flux has shown a continuous rise. Below, we discuss the results obtained from our continuing multi-wavelength observational campaign.

3.1. Evolution of 0.3–2 keV and 2–10 keV X-Ray Fluxes, the UV Flux Density, and the Photon Index

The soft X-ray flux showed considerable variability over a timescale of months to weeks in its postflare state (after 2021 October, when it reached the preflare state for the first time). It showed a rise and then a drop after that. On 2022 May 20, it reached its preflare value of $\sim 9 \times 10^{-12}$ erg cm^{-2} s^{-1} again. After this date, the flux showed a steady rise (see Figure 2, panel (2)) for 11 straight months. Nevertheless, the biweekly Swift observations have captured significant variability on a timescale of days. As of 2023 May 5, the soft X-ray flux level is ∼five times that of its preflare value.

Table 6
Optical Emission-line Properties Measured in the LDT Spectrum

Line ID	Center Wavelength (Å)	Flux_{obs} (erg s^{-1} cm^{-2}) $\times 10^{-15}$	$\text{Flux}_{\text{dered}}$ (erg s^{-1} cm^{-2}) $\times 10^{-15}$	FWHM (km s^{-1})	Comments[a]
[O II]3727	3727.49 ± 0.26	2.52 ± 0.28	3.48 ± 0.39	710.6 ± 60.4	Higher (48%)
He IIII4686	4687.99 ± 0.85	0.74 ± 0.19	0.96 ± 0.25	676.1 ± 135.2	Same
Hb	4862.10 ± 0.72	1.25 ± 0.29	1.61 ± 0.37	821.6 ± 153.0	Same
[O III]4959	4960.92 ± 0.06	2.33 ± 0.05	2.97 ± 0.07	556.5 ± 9.4	Higher (52%)
[O III]5007	5008.87 ± 0.06	7.07 ± 0.16	9.00 ± 0.20	556.5 ± 9.4	Higher (52%)
[N II]6548	6550.10 ± 0.26	0.57 ± 0.07	0.68 ± 0.08	390.5 ± 41.4	Same
Ha	6565.23 ± 0.15	5.13 ± 0.21	6.03 ± 0.25	537.3 ± 17.2	Same
[N II]6584	6585.51 ± 0.26	1.73 ± 0.22	2.04 ± 0.26	390.5 ± 41.4	Same
[S II]6716	6718.03 ± 1.81	0.30 ± 0.11	0.35 ± 0.13	374.3 ± 75.0	Same
[S II]6731	6735.27 ± 0.77	0.56 ± 0.15	0.65 ± 0.18	374.3 ± 75.0	Same

Note.
[a] Compared to the 2021 GTC observation (Laha et al. 2022).

The hard X-ray flux had reached its preflare value much earlier than the soft flux and had shown some variability throughout our campaign. But we do not detect any significant continuous rise of the flux above the preflare value like the soft flux. From Figure 2, panel (1) we note that the 2–10 keV flux showed a rise (by a factor of ∼2) in 2023 January. We note that the flux variation and the overall increase in the soft band over the last year is more significant compared to the hard band (see Figure 1).

The UVW2 flux density of 1ES 1927+654 was monitored using Swift-UVOT, and we quote the UVW2 band for consistency with the literature (although we use all the wavelength bands when we estimate L_{bol}). The UVW2 flux density shows minimal variations in the postflare state, in particular during the soft X-ray rise from 2022 May 20. The UV flux density values show a $\leqslant$30% variability over a year-long timescale, with a mean value of 1.96×10^{-15} and a standard deviation of 0.19×10^{-15} (in units of erg cm^{-2} s^{-1} Å^{-1}), respectively, and they are shown in Figure 2, panel (4). Here, we also note that the UVW2 flux level has not yet reached the preflare value of $1.34 \pm 0.03 \times 10^{-15}$ erg cm^{-2} s^{-1} Å^{-1}. See Table 2 for details. As discussed earlier, we estimated the UV band luminosity in the range (0.01–100) eV using the multiband photometric data from Swift-UVOT.

After the coronal reappearance, when the source reached its preflare state, the power-law photon index Γ has been more or less stable around the preflare value (Γ ∼ 2.2–2.6) and remained consistent within 3σ errors, even during the current bright soft state.

3.2. Evolution of λ_{Edd}

We find that the Eddington ratio ($\lambda_{\text{Edd}} = L_{\text{bol}}/L_{\text{Edd}}$) for this source was as high as $\lambda_{\text{Edd}} \sim 0.53$ (five times that of the preflare state) when the X-ray flux was the highest during the "initial flare" in 2019 November (see Table 7), and then it dropped to the preflare value ($\lambda_{\text{Edd}} \sim 0.09$) and stayed the same until the soft X-ray flux started to rise in 2022 May. Over a period of months, we see a gradual rise in the Eddington ratio, with the current value of $\lambda_{\text{Edd}} \sim 0.25$, half of the bright flux state in the "initial flare." This increase in the Eddington ratio is solely due to the rise in the soft X-ray flux and not due to the contribution from UV.

Figure 3 shows the relation between λ_{Edd} and the Γ. We do not see any strong correlation between these two parameters if we consider the observations during the postflare bright soft states (S33–S78). We find that the Γ varies within a narrow range of values, with a considerable spread in λ_{Edd}.

3.3. Correlations between SE, the Coronal Emission, and the UV Flux

We find a significant correlation between $F_{0.3\text{–}2.0\ \text{keV}}$ and $F_{2\text{–}10\ \text{keV}}$ in the postflare bright soft state of the source. The right panel of Figure 4 shows the correlation between these two quantities for the observations S33–S78, when the soft X-ray flux steadily increased (green data points). In comparison, we note that there was no correlation between the soft and hard X-rays during the "initial flare," where the nonparametric Spearman rank correlation coefficient is 0.60, with a confidence level ∼98.0% (see the left panel of Figure 4). To understand if there is indeed any relation between the SE and the power-law emission (in the current bright soft state), we correlated the respective fluxes obtained from the best-fit models, the blackbody, and the power-law, respectively. We note that we required a blackbody component to model the SE only for the observations S49–S78. We do not find any statistically significant correlation, as shown in the left panel of Figure 5. This indicates that the SE and power-law variations are independent of each other, and the apparent correlation between the 0.3–2 keV versus 2–10 keV flux is driven by the power-law component, which is very soft (Γ ∼ 2.5–3). Similarly, we find no correlations between the UV and power-law flux and the UV and blackbody flux (see the middle and right panels of Figure 5).

We also checked for individual soft X-ray flares between the different observations and found, e.g., that the soft X-ray has flared by a factor of a few times in the span of a few days: between S45 and S46, S48 and S49, S50 and S51, and S65 and S66 (see Table 2). However, the hard X-ray flux did not always show an increase corresponding to a soft X-ray increase, e.g., between S50 and S51, the soft X-ray flux increased, but the hard X-ray flux decreased. This is demonstrated in the lack of correlation between the SE flux and the power-law flux.

3.4. Evolution of Hardness Ratio

Interestingly, the hardness ratio (HR; defined as $F_{2\text{–}10.0\ \text{keV}}/F_{0.3\text{–}2.0\ \text{keV}}$) for this source always varied between 0.002 ± 0.001 (during the initial flare S01) to 0.500 ± 0.044 (during S36). If we compare these values to the preflare value

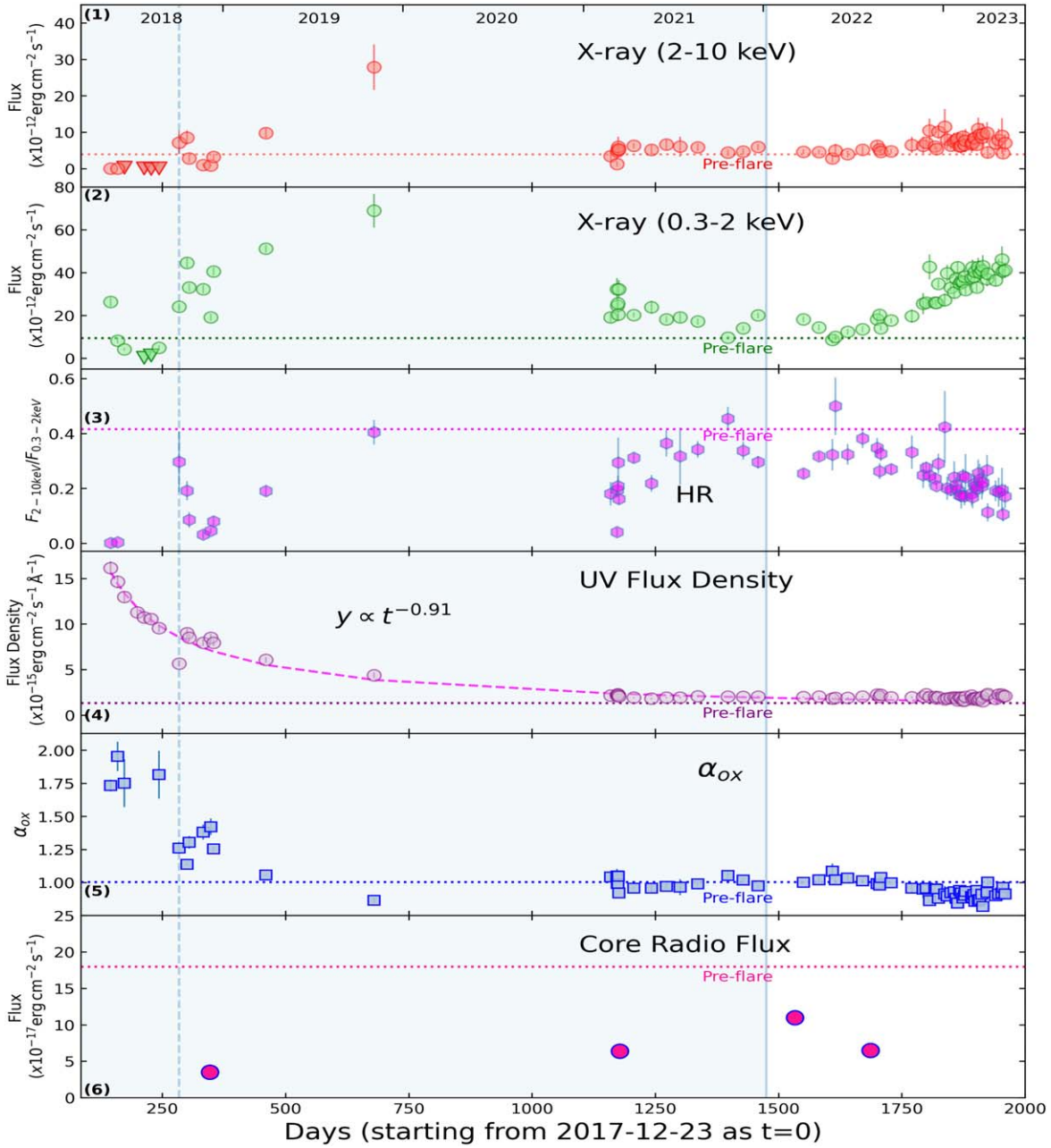

Figure 1. The light curves of the X-ray, UV, and radio parameters of the central engine of the AGN 1ES1927+654, as observed by Swift and VLBA (see Tables 2 and 3 for details). The shaded region corresponds to the observations discussed in our earlier work (Laha et al. 2022), but we have included them here for the sake of completeness and to track the long-term nature of this source. The rest of the figure refers to the new observations used in this work. The start date of the light curve is 2017 December 23, corresponding to the burst date reported by Trakhtenbrot et al. (2019). The *X*-axis is in units of days elapsed from the start date. The dotted horizontal lines in every panel refer to the preflare values (in 2011). The inverted triangles are the upper limits. The X-ray flux is in units of 10^{-12} erg cm^{-2} s^{-1}, corrected for Galactic absorption. From top to bottom, the panels are as follows: (1) the 2–10 keV X-ray flux; (2) the 0.3–2 keV X-ray flux; (3) the HR: $F_{2-10\ \mathrm{keV}}/F_{0.3-2\ \mathrm{keV}}$; (4) the UV (UVW2) flux density (in units of 10^{-15} erg cm^{-2} s^{-1}Å^{-1}); (5) the α_{OX}; and (6) the core radio flux (<1 pc spatial resolution). Note that the vertical line corresponds to the observation S8, where the X-ray corona jumps back (created) after being destroyed, there is a dip in the UV flux by a factor of 2, and the X-ray spectra also become harder (panel (3)).

of 0.417 ± 0.021 (X1), we see the HR has always been either lower or within errors compared to the preflare value. During the "initial flare," the HR showed both hard when bright (while rising) and soft when bright (while coming back) behavior. The HR increased at the observation when the corona was revived in 2018 October. In the postflare state, during observations S15–S33, when the source showed minimal X-ray variations, the HR still varied considerably within this range. See Figure 1, panel (3). We do not detect any fixed pattern for the HR variability in response to the X-ray flux changes. Nor do we find any significant correlation between $L_{0.3-10\ \mathrm{keV}}$ and HR (see Figure 6). During the recent bright soft state observed from S33, the HR varied considerably between these limits. Currently (S78), in the bright soft state, we find the HR to be ∼0.172.

3.5. Correlation between Γ and $L_{2-10\ keV}$

We plotted the power-law slope Γ and the hard X-ray luminosity ($L_{2-10\ \mathrm{keV}}$) for the bright soft state (Figure 7). It is

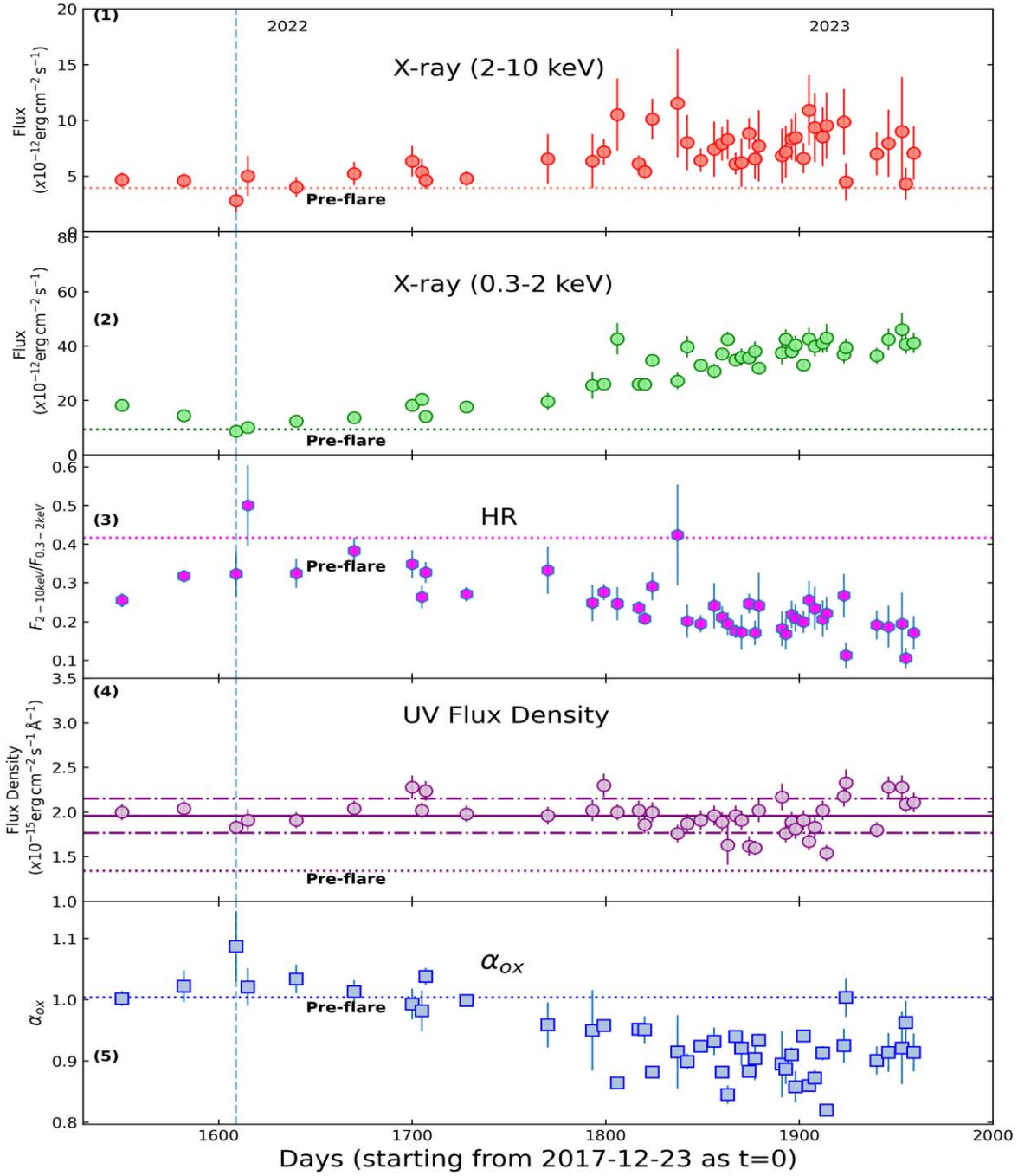

Figure 2. The zoomed-in version of the X-ray and UV light curves plotted in Figure 1, encompassing the observations S33–S78, to highlight the rise of the bright soft state of the source 1ES1927+654. The vertical dashed blue line corresponds to observation S35, when both the soft and the hard X-ray fluxes exactly matched their preflare values in 2011. See Table 2 for details. The start date (day zero) of the light curve is 2017 December 23, corresponding to the burst date reported by Trakhtenbrot et al. (2019), and the *X*-axis is in units of days elapsed from the start date. The dotted horizontal lines in each panel refer to the preflare values (in 2011). From top to bottom, the panels are as follows: (1) the X-ray 2–10 keV flux (in units of 10^{-12} erg cm^{-2} s^{-1}); (2) the X-ray 0.3–2 keV flux (in units of 10^{-12} erg cm^{-2} s^{-1}); (3) the HR: $F_{2-10\ \mathrm{keV}}/F_{0.3-2\ \mathrm{keV}}$; (4) the evolution of the UV (UVW2) flux density, along with the mean (1.96), denoted by a solid line, and standard deviations (0.19), denoted by dashed–dotted lines (in units of 10^{-15} erg cm^{-2} s^{-1}Å^{-1}); and (5) the α_{OX} values during observations S33–S78 are plotted.

evident from the figure that in the postflare state, the power-law slope is insensitive to the variations in the 2–10 keV luminosity.

3.6. The Evolution of α_{OX}

The ratio between the X-ray and UV, which we refer to as α_{OX}, is calculated from the ratio of the monochromatic fluxes in the UV (2500 Å) and X-rays (2 keV), i.e., $\alpha_{\mathrm{OX}} = -0.385 \log(F_{2\ \mathrm{keV}}/F_{2500\ \text{Å}})$ (Tananbaum et al. 1979; Lusso et al. 2010). This is an important diagnostic parameter to understand if the accretion disk and the X-ray-emitting corona are physically connected. The α_{OX} had attained a very high value of ∼2 during the "initial flare"; however, in the postflare state, the values are mostly consistent with that of the preflare state. In the recent bright soft state, the α_{OX} has dropped. This is because there is no change in the UV flux, while the X-ray flux has increased. Figure 8 shows the relation between α_{OX} and $L_{2500\ \text{Å}}$ and we find that the recent bright soft state data

Table 7
The Evolution of the Disk Temperature and $\lambda_{\rm Edd}$ Estimated from the Swift and XMM-Newton UV and X-ray Observations of 1ES 1927+654

Obs	Diskbb	$L_{\rm UV}$	$L_{\rm X}$	$L_{\rm Bol}$	$\lambda_{\rm Edd}$
Id	in eV	10^{43} erg s^{-1}	10^{43} erg s^{-1}	$L_{\rm UV}+L_{\rm X}$	$L_{\rm Bol}/L_{\rm Edd}$
X1	03 ± 01	$0.28^{+0.05}_{-0.05}$	$0.86^{+0.01}_{-0.01}$	$1.14^{+0.06}_{-0.06}$	0.09 ± 0.01
S01	08 ± 01	$2.10^{+0.07}_{-0.07}$	$1.70^{+0.14}_{-0.14}$	$3.80^{+0.21}_{-0.21}$	0.29 ± 0.02
S02	08 ± 02	$1.92^{+0.08}_{-0.07}$	$0.54^{+0.09}_{-0.09}$	$2.46^{+0.17}_{-0.16}$	0.19 ± 0.01
S03	06 ± 02	$1.81^{+0.05}_{-0.06}$	$0.01^{+0.01}_{-0.01}$	$1.82^{+0.06}_{-0.07}$	0.14 ± 0.01
S04	08 ± 01	$1.98^{+0.05}_{-0.04}$	$0.01^{+0.01}_{-0.01}$	$1.99^{+0.06}_{-0.05}$	0.15 ± 0.01
S05	04 ± 02	$1.56^{+0.05}_{-0.05}$	$0.01^{+0.01}_{-0.01}$	$1.57^{+0.06}_{-0.06}$	0.12 ± 0.01
S06	08 ± 03	$1.38^{+0.06}_{-0.05}$	$0.01^{+0.01}_{-0.01}$	$1.39^{+0.07}_{-0.06}$	0.11 ± 0.01
S07	07 ± 04	$1.28^{+0.05}_{-0.06}$	$0.01^{+0.01}_{-0.01}$	$1.29^{+0.06}_{-0.07}$	0.10 ± 0.01
S08	03 ± 02	$1.00^{+0.09}_{-0.07}$	$2.01^{+0.30}_{-0.30}$	$3.01^{+0.39}_{-0.37}$	0.23 ± 0.03
S09	10 ± 04	$1.11^{+0.05}_{-0.04}$	$3.42^{+0.28}_{-0.28}$	$4.53^{+0.33}_{-0.32}$	0.35 ± 0.03
S10	13 ± 07	$1.08^{+0.04}_{-0.04}$	$2.31^{+0.18}_{-0.18}$	$3.39^{+0.22}_{-0.22}$	0.26 ± 0.02
S11	12 ± 06	$0.99^{+0.03}_{-0.02}$	$2.15^{+0.16}_{-0.16}$	$3.16^{+0.19}_{-0.18}$	0.24 ± 0.01
S12	12 ± 06	$1.06^{+0.03}_{-0.03}$	$1.29^{+0.12}_{-0.12}$	$2.35^{+0.15}_{-0.15}$	0.18 ± 0.01
S13	08 ± 03	$1.03^{+0.03}_{-0.03}$	$2.82^{+0.18}_{-0.18}$	$3.85^{+0.21}_{-0.21}$	0.30 ± 0.02
S14	07 ± 04	$0.82^{+0.04}_{-0.04}$	$3.92^{+0.18}_{-0.20}$	$4.74^{+0.22}_{-0.24}$	0.37 ± 0.02
S14A	07 ± 04	$0.60^{+0.05}_{-0.05}$	$6.23^{+0.88}_{-0.92}$	$6.83^{+0.93}_{-0.97}$	0.53 ± 0.07
S33	05 ± 02	$0.28^{+0.03}_{-0.02}$	$1.47^{+0.13}_{-0.13}$	$1.75^{+0.15}_{-0.16}$	0.14 ± 0.01
S34	04 ± 03	$0.30^{+0.03}_{-0.02}$	$1.23^{+0.13}_{-0.13}$	$1.53^{+0.15}_{-0.16}$	0.12 ± 0.01
S35	05 ± 03	$0.27^{+0.05}_{-0.04}$	$0.74^{+0.18}_{-0.18}$	$1.01^{+0.22}_{-0.23}$	0.08 ± 0.02
S36	06 ± 02	$0.28^{+0.03}_{-0.03}$	$0.97^{+0.20}_{-0.20}$	$1.25^{+0.22}_{-0.23}$	0.10 ± 0.02
S37	04 ± 03	$0.29^{+0.04}_{-0.03}$	$1.06^{+0.14}_{-0.14}$	$1.35^{+0.18}_{-0.17}$	0.10 ± 0.02
S38	05 ± 03	$0.31^{+0.03}_{-0.03}$	$1.21^{+0.16}_{-0.16}$	$1.52^{+0.19}_{-0.18}$	0.12 ± 0.02
S39	08 ± 05	$0.29^{+0.03}_{-0.03}$	$1.58^{+0.22}_{-0.22}$	$1.87^{+0.25}_{-0.24}$	0.14 ± 0.02
S40	05 ± 02	$0.28^{+0.05}_{-0.05}$	$1.66^{+0.21}_{-0.21}$	$1.94^{+0.26}_{-0.25}$	0.15 ± 0.02
S41	08 ± 04	$0.28^{+0.03}_{-0.03}$	$1.21^{+0.12}_{-0.12}$	$1.49^{+0.15}_{-0.14}$	0.12 ± 0.01
S42	03 ± 01	$0.32^{+0.02}_{-0.03}$	$1.45^{+0.12}_{-0.12}$	$1.77^{+0.14}_{-0.15}$	0.14 ± 0.01
S43	03 ± 01	$0.33^{+0.03}_{-0.03}$	$1.69^{+0.30}_{-0.29}$	$2.02^{+0.33}_{-0.32}$	0.16 ± 0.02
S44	04 ± 02	$0.29^{+0.04}_{-0.04}$	$1.92^{+0.37}_{-0.35}$	$2.21^{+0.41}_{-0.39}$	0.17 ± 0.03
S45	03 ± 02	$0.33^{+0.05}_{-0.05}$	$2.14^{+0.20}_{-0.21}$	$2.47^{+0.25}_{-0.26}$	0.19 ± 0.02
S46	05 ± 03	$0.30^{+0.04}_{-0.03}$	$3.22^{+0.54}_{-0.55}$	$3.52^{+0.58}_{-0.58}$	0.27 ± 0.04
S47	03 ± 01	$0.30^{+0.04}_{-0.04}$	$2.07^{+0.14}_{-0.13}$	$2.37^{+0.18}_{-0.17}$	0.18 ± 0.02
S48	03 ± 01	$0.30^{+0.05}_{-0.04}$	$2.01^{+0.16}_{-0.16}$	$2.31^{+0.21}_{-0.20}$	0.18 ± 0.02
S49	03 ± 02	$0.37^{+0.05}_{-0.05}$	$2.89^{+0.23}_{-0.24}$	$3.26^{+0.28}_{-0.29}$	0.25 ± 0.02
S50	04 ± 02	$0.30^{+0.07}_{-0.05}$	$2.49^{+0.40}_{-0.40}$	$2.79^{+0.47}_{-0.45}$	0.22 ± 0.03
S51	05 ± 03	$0.27^{+0.06}_{-0.04}$	$3.07^{+0.40}_{-0.41}$	$3.34^{+0.45}_{-0.45}$	0.26 ± 0.03
S52	08 ± 04	$0.27^{+0.05}_{-0.05}$	$2.53^{+0.16}_{-0.17}$	$2.80^{+0.21}_{-0.22}$	0.22 ± 0.02
S53	06 ± 03	$0.27^{+0.05}_{-0.03}$	$2.45^{+0.34}_{-0.34}$	$2.72^{+0.39}_{-0.37}$	0.21 ± 0.03
S54	03 ± 02	$0.30^{+0.05}_{-0.05}$	$2.90^{+0.24}_{-0.24}$	$3.20^{+0.29}_{-0.29}$	0.25 ± 0.02
S55	04 ± 02	$0.30^{+0.05}_{-0.05}$	$3.39^{+0.29}_{-0.31}$	$3.69^{+0.34}_{-0.36}$	0.28 ± 0.03
S56	03 ± 01	$0.28^{+0.03}_{-0.03}$	$2.37^{+0.15}_{-0.17}$	$2.65^{+0.18}_{-0.20}$	0.20 ± 0.02
S57	03 ± 01	$0.33^{+0.05}_{-0.05}$	$2.71^{+0.36}_{-0.35}$	$3.04^{+0.41}_{-0.40}$	0.23 ± 0.03
S58	03 ± 01	$0.32^{+0.08}_{-0.06}$	$2.87^{+0.22}_{-0.24}$	$3.19^{+0.30}_{-0.30}$	0.25 ± 0.02
S59	02 ± 01	$0.30^{+0.06}_{-0.05}$	$2.87^{+0.36}_{-0.34}$	$3.17^{+0.42}_{-0.39}$	0.24 ± 0.03
S60	04 ± 02	$0.44^{+0.04}_{-0.04}$	$2.55^{+0.34}_{-0.32}$	$2.99^{+0.38}_{-0.36}$	0.23 ± 0.03
S61	06 ± 03	$0.30^{+0.04}_{-0.03}$	$2.85^{+0.40}_{-0.42}$	$3.15^{+0.44}_{-0.45}$	0.24 ± 0.03
S62	03 ± 01	$0.32^{+0.06}_{-0.06}$	$3.20^{+0.38}_{-0.36}$	$3.52^{+0.44}_{-0.42}$	0.27 ± 0.03
S63	04 ± 02	$0.30^{+0.04}_{-0.03}$	$2.98^{+0.29}_{-0.27}$	$3.28^{+0.33}_{-0.30}$	0.25 ± 0.02
S64	03 ± 02	$0.28^{+0.04}_{-0.04}$	$3.40^{+0.36}_{-0.38}$	$3.68^{+0.40}_{-0.42}$	0.28 ± 0.03
S65	04 ± 01	$0.31^{+0.03}_{-0.04}$	$2.55^{+0.22}_{-0.22}$	$2.86^{+0.26}_{-0.25}$	0.22 ± 0.02
S66	02 ± 01	$0.32^{+0.06}_{-0.05}$	$3.24^{+0.37}_{-0.37}$	$3.56^{+0.42}_{-0.43}$	0.27 ± 0.03
S67	05 ± 03	$0.28^{+0.05}_{-0.04}$	$3.17^{+0.44}_{-0.44}$	$3.55^{+0.49}_{-0.48}$	0.27 ± 0.04
S68	04 ± 02	$0.30^{+0.05}_{-0.05}$	$3.19^{+0.40}_{-0.40}$	$3.49^{+0.45}_{-0.45}$	0.27 ± 0.04
S69	02 ± 02	$0.29^{+0.05}_{-0.04}$	$3.38^{+0.50}_{-0.52}$	$3.67^{+0.55}_{-0.56}$	0.28 ± 0.04
S71	05 ± 03	$0.33^{+0.05}_{-0.04}$	$3.01^{+0.41}_{-0.39}$	$3.31^{+0.46}_{-0.43}$	0.26 ± 0.03
S72	03 ± 01	$0.34^{+0.05}_{-0.04}$	$2.83^{+0.32}_{-0.30}$	$3.15^{+0.37}_{-0.34}$	0.24 ± 0.03

Table 7
(Continued)

Obs	Diskbb	L_{UV}	L_X	L_{Bol}	λ_{Edd}
S73	03 ± 01	$0.29^{+0.05}_{-0.04}$	$2.80^{+0.30}_{-0.32}$	$3.07^{+0.35}_{-0.36}$	0.24 ± 0.03
S74	08 ± 04	$0.28^{+0.02}_{-0.01}$	$3.24^{+0.46}_{-0.44}$	$3.50^{+0.48}_{-0.45}$	0.27 ± 0.04
S76	05 ± 02	$0.30^{+0.04}_{-0.03}$	$3.54^{+0.72}_{-0.70}$	$3.81^{+0.76}_{-0.73}$	0.29 ± 0.06
S77	04 ± 02	$0.30^{+0.02}_{-0.02}$	$2.89^{+0.30}_{-0.32}$	$3.17^{+0.32}_{-0.34}$	0.24 ± 0.03
S78	04 ± 02	$0.33^{+0.04}_{-0.04}$	$3.10^{+0.38}_{-0.40}$	$3.40^{+0.42}_{-0.44}$	0.26 ± 0.03

Note. The Eddington rate for an SMBH with a mass of $10^6 M_\odot$ is 1.3×10^{44} erg s^{-1}. The X-ray luminosity is calculated from the 0.3–10 keV energy band by adding the soft and hard X-ray flux. During the lowest luminosity phase (S03–S07), we assumed an upper limit of 10^{41} erg s^{-1} for the X-ray flux.

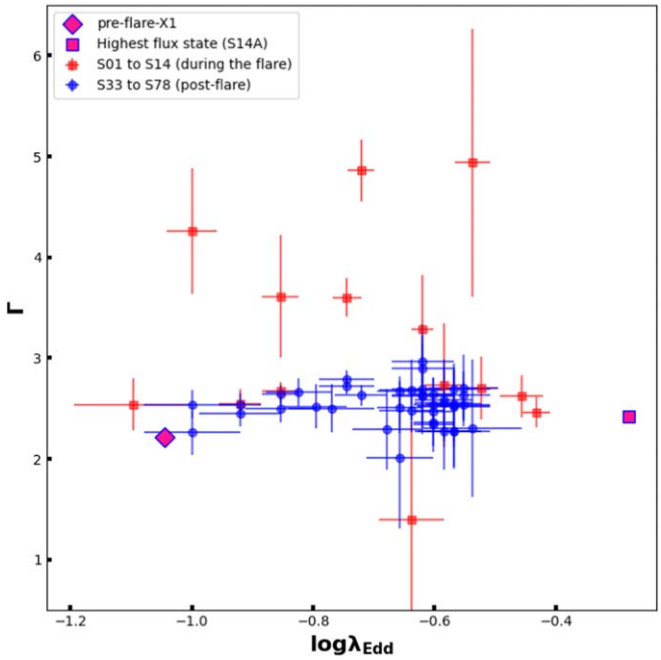

Figure 3. The evolution of $\log(\lambda_{Edd})$ and the power-law slope Γ of the CL-AGN 1ES 1927+654 during the initial flare (red squares) and the postflare state (blue circles). See Table 7 for details. We do not see any correlation between these parameters either during the initial flare or the postflare states.

points denoted by the blue dots deviate considerably from standard AGN behavior. We plot the "highest flaring state" data point on this plot to give an idea of where the source was in this phase space during the "initial flare."

3.7. The 5 GHz Radio Observations

The PS radio flux density at 5 GHz was at a minimum (a factor of 4 lower than the preflare value) when the X-rays were just starting to increase. Over a period of the next one thousand days, the radio flux density gradually increased (Yang et al. 2022), which coincided with the time period when the UV and X-rays returned to their preflare values (see Figure 1). However, the latest VLBA observation in 2022 August showed a decrease in the core radio flux density compared to 2021 March. This decrease also coincides with the latest rise in the soft X-ray flux (the bright soft state). The radio flux density could be related to either the hard or the soft X-ray or both in a more complex way.

The ratio between the radio and the X-ray (known as the GB relation) has been plotted in Figure 9. We find that the ratio constantly decreased during the initial flare, it picked up a little in 2021, and then it started decreasing again. The values of the ratio are well within the spread of the values found typically in radio-quiet AGNs in the Palomar-Green sample studied by Laor & Behar (2008). We see only a minor change in the morphology (the size became smaller) of the extended emission, but not in intensity.

3.8. The Optical Spectra

Both the optical spectra from LDT and HCT show mostly narrow emission lines, as reported in our earlier work. We also detect broad Hα with a typical FWHM of 1172 ± 327 km s^{-1}. We do not see any change in the narrow or broad emission-line intensities and the line ratios from our earlier work (Laha et al. 2022), except for O III, where the line intensity has nearly doubled. The reduced spectra and the best-fit model from HCT are shown in Figures 10 and 11, respectively, showing line intensities consistent with Laha et al. (2022).

4. Discussion

We have followed up the CL-AGN 1ES 1927+654 with X-ray and UV observations with Swift, radio observations from VLBA, and optical observations from LDT and HCT. Our earlier paper (Laha et al. 2022) reported the observations until 2021 December 31, encompassing the entire phase of the "initial flare." Here we report the multiwavelength observations from 2022 January 1 until 2023 May 5, particularly highlighting the recent bright soft state of the source. In light of our multiwavelength observations, we address the following scientific questions.

4.1. The Recent Bright Soft State and the Origin of the SE

The SE is the excess emission (over the power law) in the soft band 0.3–2 keV in an AGN spectrum, which typically takes the shape of a blackbody with temperatures ranging from 0.1 to 0.3 keV. The origin of the SE is still highly debated (Noda & Done 2018; García et al. 2019; Ghosh & Laha 2020, 2021), as different sources show different spectral and timing behaviors of the SE with respect to the other bands of the AGN continuum, such as the UV (accretion disk) and 2–10 keV (power law). The two most popular models describing the SE are: (a) thermal Comptonization from the warm ($kT_e \sim 0.1$–0.5 keV), optically thick ($\tau \sim 10$–20) corona (Mehdipour et al. 2011; Done et al. 2012; Ghosh et al. 2018; Petrucci et al. 2018, 2020); and (b) reflection of the primary continuum from the ionized disk (García et al. 2014, 2019; Ghosh et al. 2016).

The thermal Comptonization assumes the existence of a warm ($kT \sim 0.1$ keV), optically thick medium above the accretion disk. A fraction of the accretion disk photons interact with this plasma and are upscattered to create the blackbody-

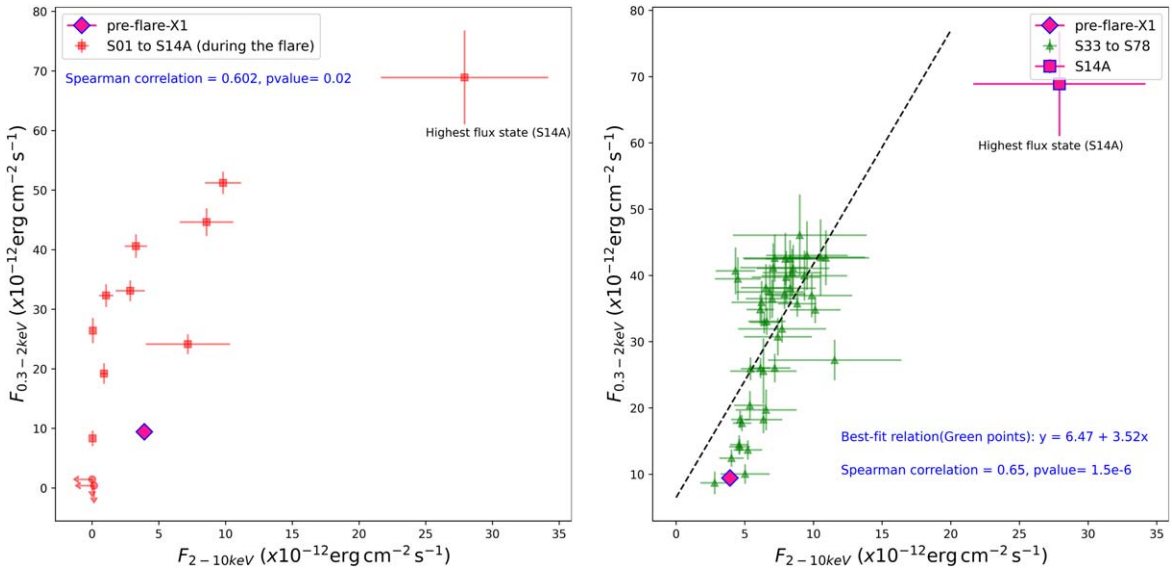

Figure 4. Left: the relation between the soft X-ray (0.3–2 keV) and hard X-ray (2–10 keV) fluxes during the initial flare. The red circles denote the X-ray flaring period covering 2018–2019 (observations S01–S14A). The upper limits denote the lowest state in X-rays in both axes in the lower left corner of the figure. The soft and the hard X-rays do not show any significant correlation. Right: the same as the left, but for the new observations (S33–S78) encompassing the bright soft state, which show a significant correlation between the soft and hard X-ray flux, driven by the power-law flux alone, due to the soft nature of the source. The best-fit linear regression fit gives us $y = 6.47 + 3.52x$, with a Spearman rank correlation coefficient = 0.65 and a statistical significance >99.99%.

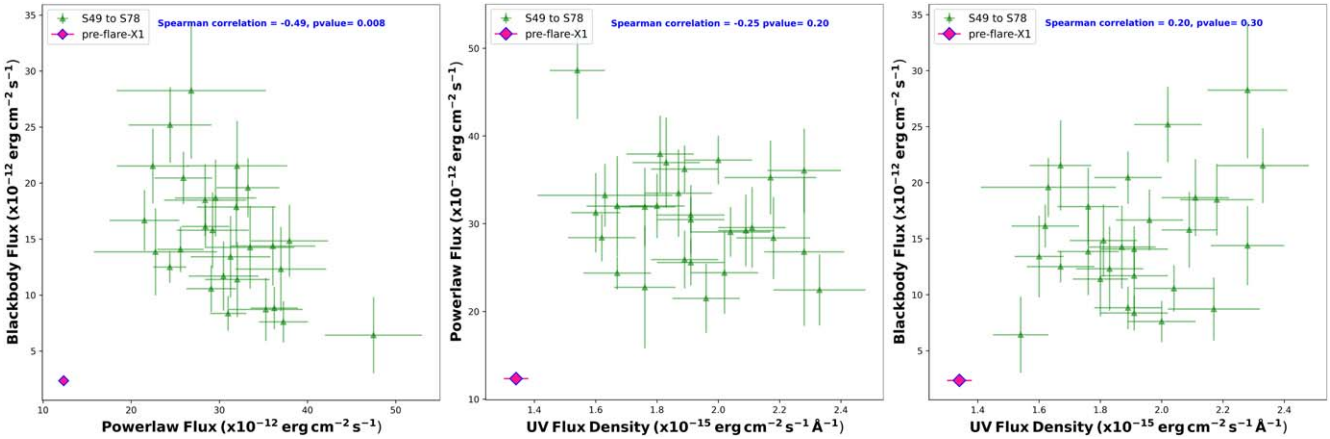

Figure 5. Left: the power-law (0.3–10 keV) flux vs. the blackbody (0.3–10 keV) flux plot during the bright soft state (i.e., observations S49–S78) exhibits no significant correlation. The bright soft state is plotted in green, and the preflare XMM data are plotted in magenta for comparison. Middle: the power-law 0.3–10 keV flux vs. the UVW2 flux density plot. Right: the blackbody 0.3–10 keV flux vs. the UVW2 flux density plot during the same period as in the left panel similarly shows no statistically significant correlation.

shaped SE. Therefore, this model points toward a direct link between the UV and SE flux. This model predicts that an increase in the UV should be related to an increase in the soft X-rays and vice versa.

The relativistic reflection, on the other hand, assumes that the SE arises out of the reflection of the hard X-ray photons from the primary continuum emission from the ionized accretion disk. The individual emission lines arising out of the reflection get smoothed out (broadened beyond detection) by gravitational effects. This model, therefore, assumes a direct link between the 2–10 keV flux and the SE flux.

The SE behavior in source 1ES1927+654 is very unique. During the "initial flare" (during 2017–2019, reported in Ricci et al. 2021; Laha et al. 2022; Masterson et al. 2022), the source started off very soft, when the UV was gradually decreasing. When the 2–10 keV band X-rays completely vanished, there were still some traces of the SE, as detected by XMM-Newton (Ricci et al. 2021). This phase of the SE was characterized by an unusually varying lower-temperature ($kT \sim 0.08$–0.1 keV) blackbody. The temperature was lower than that usually measured for this source in the preflare state ($kT \sim 0.2$ keV). The presence of SE in the absence of a power-law component is inconsistent with the reflection scenario because, without the primary power law, there should not be any reflection in the first place. This is also unusual in the warm Comptonization scenario, because the UV flux was very high at the time when the SE was the lowest, unless the warm Comptonizing corona had also vanished in some way. When the X-rays revived with a flare in 2018 October (see Figure 1), the UV was still monotonically decreasing, with a power-law decline $y \propto t^{-0.91}$. There was no correlation between the UV and X-ray fluxes, or even between the soft and hard X-ray fluxes (see Figure 4, left panel). These results make it hard to

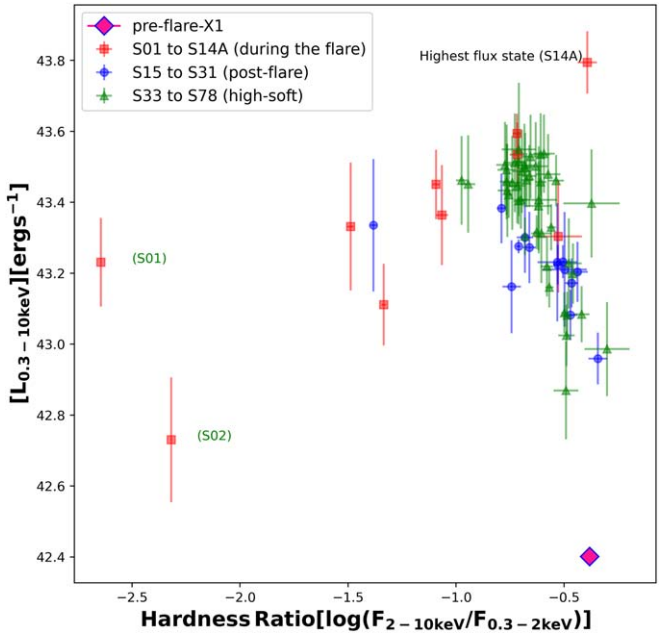

Figure 6. Hardness intensity diagram for 1ES 1927+654. The "initial flare" S01–S14A observations are plotted as red squares. The postflare states S15–S31 (when the source got back to the preflare state) are plotted as blue circles. The bright soft state S33–S78 is plotted as green triangles (see Table 2 for details).

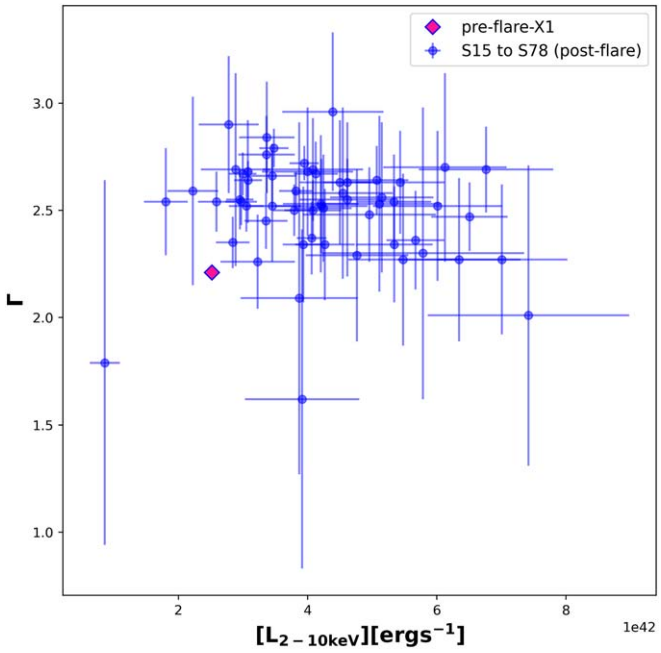

Figure 7. The photon index Γ and the 2–10 keV X-ray luminosity plot during the bright soft state that is S33–S78. The Γ is relatively insensitive to the hard X-ray luminosity.

describe the SE of this source with either of the two models mentioned above.

During the recent bright soft state since 2022 May, which became more prominent in 2022 December, we find that the UVW2 flux density changes are confined within a fluctuation range of $\leqslant$30%. The mean value of the UV flux in the bright soft state is 1.96×10^{-15}, with a standard deviation of 0.19×10^{-15} (in units of erg cm^{-2} s^{-1}Å^{-1}). While the UV flux shows minimal change, the soft X-ray flux has increased by a factor of 5 compared to the preflare state. The hard X-ray flux has also increased by a factor of ∼2, but has shown substantial fluctuations in the latest observations (see Figure 2 for details). We do not see any correlations between the UV and soft X-rays and the UV and hard X-rays (see Figure 12). This is in agreement with the lack of correlation observed between the SE flux (modeled by the blackbody) and the coronal flux (modeled by the power law) in the recent bright soft state (Figure 5). These results are inconsistent with both the models describing the SE as the reflection from the ionized disk and/or the thermal Comptonization scenario.

Previous studies using broadband spectroscopy with XMM-Newton concluded that the 1 keV emission feature (detected in XMM-Newton and NICER observations) could arise out of the reflection of the hard X-ray photons of the accretion disk (Masterson et al. 2022). They suggested that relativistic reflection happened during the TDE, resulting in the 1 keV emission line. The spectroscopic fits could not distinguish between the thermal Comptonization and the reflection models for the origin of the SE.

Other CL-AGN sources have also shown the absence of correlation between the X-rays and the UV and between the soft and the hard X-rays. For example, Mrk 590 (Ghosh et al. 2022), where we found that the SE completely vanished when the power law and the UV were still dominant. We also note that in 1ES1927+654, since the start of the bright soft state, the Γ has not varied significantly, staying between $2.01^{+0.50}_{-0.90}$ and $2.96^{+0.36}_{-0.37}$, consistent within the large errors.

Now the question is: what is pumping the energy to the X-rays if the UV flux, and hence the standard accretion rate, is so silent? To understand this, we need to have some estimate of the energy. First, we calculate the energetics of this system in one of the shortest-variability timescales, which in this case is 4 days (the cadence of our Swift observation). We note that the highest soft and hard X-ray flux change happened between S48 and S49 (a gap of 4 days). Assuming a constant increase profile, we estimated that the soft-band energy being pumped over four days is equal to 9.7×10^{47}erg. During that time, the total hard X-ray energy being pumped is equal to 3.7×10^{47}erg, while the energy pumped in UV amounts to 1.9×10^{47}erg, which roughly equals 14% of the total X-ray energy pumped during this period.

Now let us consider the energy pumped over a longer timescale since the rise of the bright soft state phase, which is between S35 (2022 May) and S76 (2023 May). During these 11 months (344 days), the energy pumped in the soft and hard bands is 3.57×10^{50}erg and 0.59×10^{50}erg, respectively. During this one-year-long time period, the UV band did not show any significant change at all (see Figure 2), with the fluctuations being consistent within one standard deviation around the mean value. Figure 13 shows the soft and the hard X-ray band rise and the best-fit linear regression line. The integrated energy for the soft and hard bands quoted above (for 11 months) has been estimated by the area under the best-fit linear regression curve.

In addition, we can estimate the mass accretion rate required to create the luminosity in the soft X-rays from the standard accretion theory, $L = \eta \dot{M} c^2$, where L is the accretion luminosity, η is the accretion efficiency, $\dot{M}$ is the mass accretion rate, and c is the speed of light. This is assuming that whatever is creating the soft X-rays is accreting and deriving its energy from the gravitational binding energy. If we assume a value of $\eta = 0.1$ for standard AGNs, we get an accretion rate of $\sim 0.003 M_{\odot}\,\mathrm{yr}^{-1}$ needed to create this bright soft state.

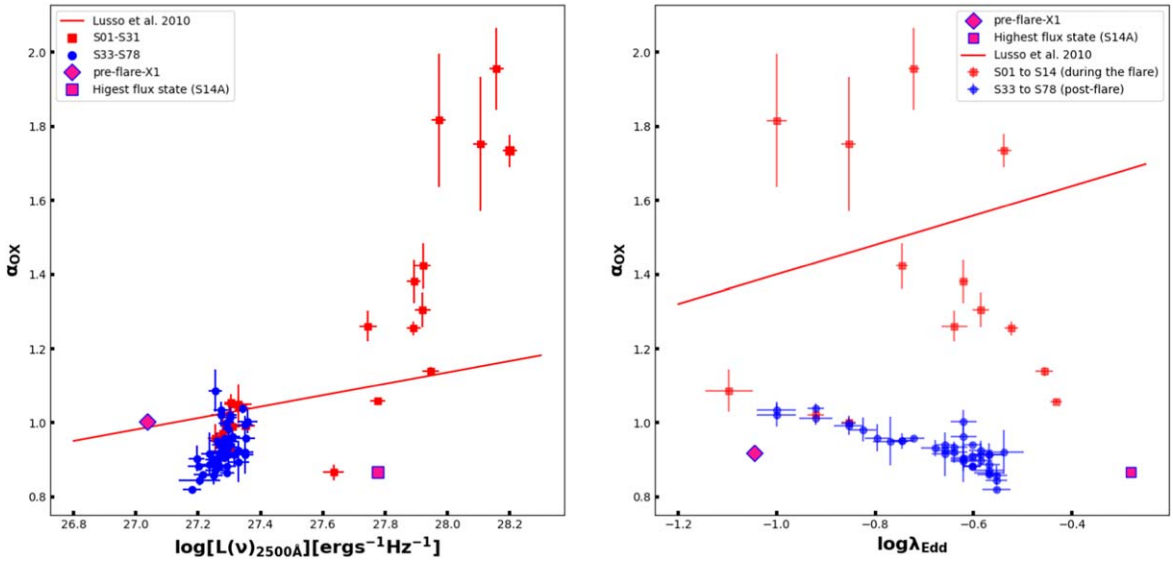

Figure 8. Left: the α_{OX} vs. $L_{2500\text{Å}}$ for the different Swift observations of the source 1ES 1927+654, as reported in Table 2 and Laha et al. (2022). The red line is the best-fit correlation from Lusso & Risaliti (2016), representing the standard AGN disk–corona relation. The pink diamond represents the 2011 pre-CL state of 1ES 1927+654. Right: the evolution of $\log(\lambda_{Edd})$ and α_{OX} during the initial flare (red squares) and the postflare state (blue circles). See Table 7 for details. The solid red line shows the generic AGN behavior, as obtained by Lusso & Risaliti (2016) for a sample of AGNs. We do not see any correlation between these parameters either during the initial flare or the postflare states.

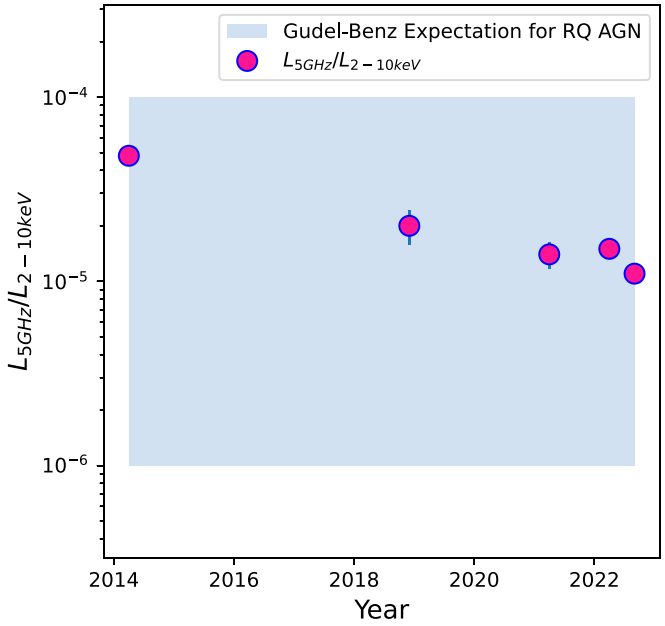

Figure 9. The light curve of the ratio of the 5 GHz monochromatic central radio luminosity with the 2–10 keV luminosity, popularly known as the GB relation. See Table 4 for details. The 0.3–2.0 keV X-ray flux vs. the 5 GHz monochromatic radio flux exhibits no correlation. See Tables 2 and 4 for the X-ray and radio flux values. The shaded region represents the standard range of the GB relation for radio-quiet AGNs.

From the energetics, it is evident that whatever is producing the SE is pumping out more energy than either the UV or hard X-ray source. Since the energy source presumably is ultimately the accretion of matter onto the SMBH, the SE-emitting region must be receiving the majority of this energy. This could mean that the SE region is either the dominant accreting flow or that there is a conduit pumping the accretion energy from the disk to the SE region, rather than radiating it inside the disk.

If warm Comptonization produced the SE, then one would expect a direct relation between the UV luminosity and the soft X-ray luminosity, e.g., as observed in NGC 3516 (Mehdipour et al. 2022), but we do not find this in 1ES 1927+654. Moreover, one would expect to observe absorption in the soft X-rays, due to the atomic opacity in the warm Comptonizing corona (García et al. 2019), which we do not see in the XMM-Newton EPIC-pn data of the source in the bright soft state (R. Ghosh et al. 2023, in preparation). The reflection scenario, on the other hand, cannot explain a weaker (∼two times) hard X-ray variation (which is the primary flux) compared to the stronger (∼five times) consistent rise of the soft X-rays, with the soft X-rays gaining ∼10 times more energy than the primary power law in a matter of 11 months. This is also true if we see the initial flare (Laha et al. 2022), where no correlation between the soft and hard X-ray was found.

Therefore, in this source, we need a different mechanism to produce the SE. We conjecture that the SE in this source may not be the canonical SE we find in typical AGNs. This is supported by several observational results from both the initial flare (2017 December–2019 December) and the bright soft state (2022 May–2023 May), such as: (1) there is no correlation between the SE and other X-ray and UV components; (2) the SE is modeled by an unusually varying lower-temperature blackbody ($kT \sim 0.08$–0.1 keV) in the initial flare when the coronal emission vanished; and (3) the current consistent rise in the SE has a blackbody temperature that is mostly constant, but on the higher side ($kT \sim 0.15$–0.2 keV).

4.2. The Relation between α_{OX} versus $L_{2500\text{ Å}}$ and α_{OX} versus λ_{Edd}

The relation between α_{OX} and $L_{2500\text{ Å}}$ has been found to be tightly related for AGNs across cosmic timescales (Lusso et al. 2010; Lusso & Risaliti 2016), which implies a close relation between the accretion disk (UV) and the corona (X-ray). The left panel of Figure 8 shows the data points for the source 1ES 1927+654 during the initial flare (in red) and the bright soft state (in blue), and in neither cases does the source behavior follow the commonly detected correlation (the red

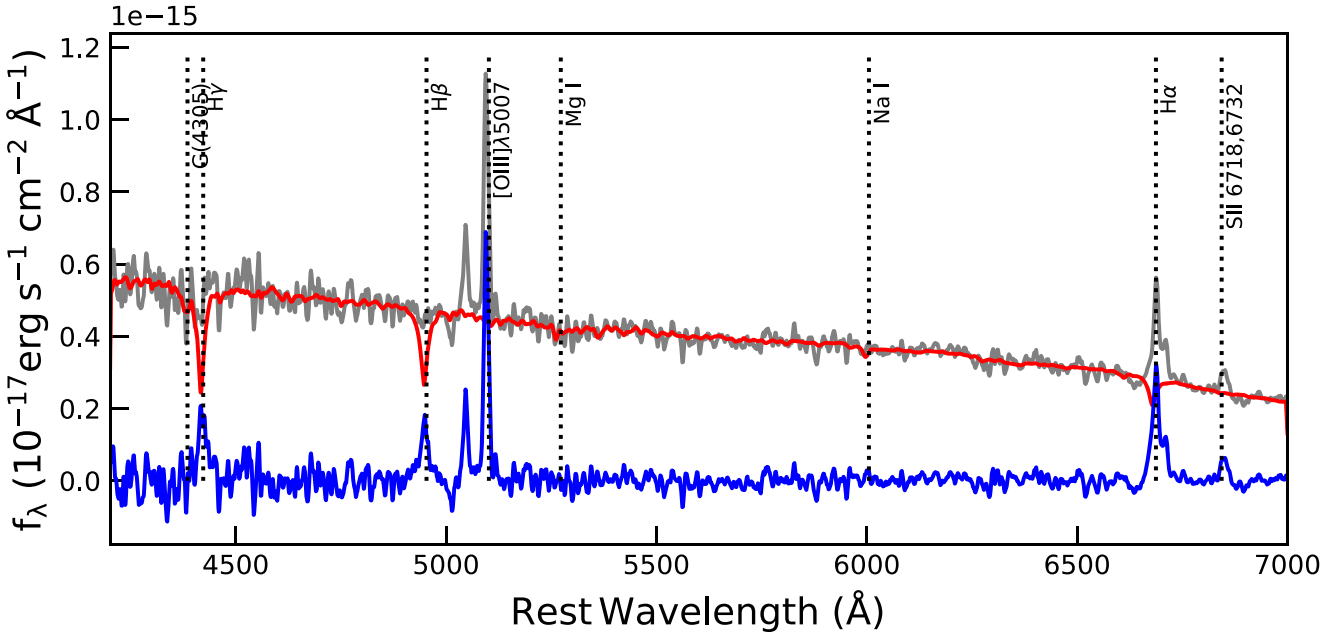

Figure 10. Optical spectrum of 1ES 1927+654 obtained with HCT. The data are shown in gray, the decomposed stellar template is shown in red, and the host-subtracted spectrum is shown in blue. The spectrum was smoothened by a 5 pixel box car for visualization purposes only.

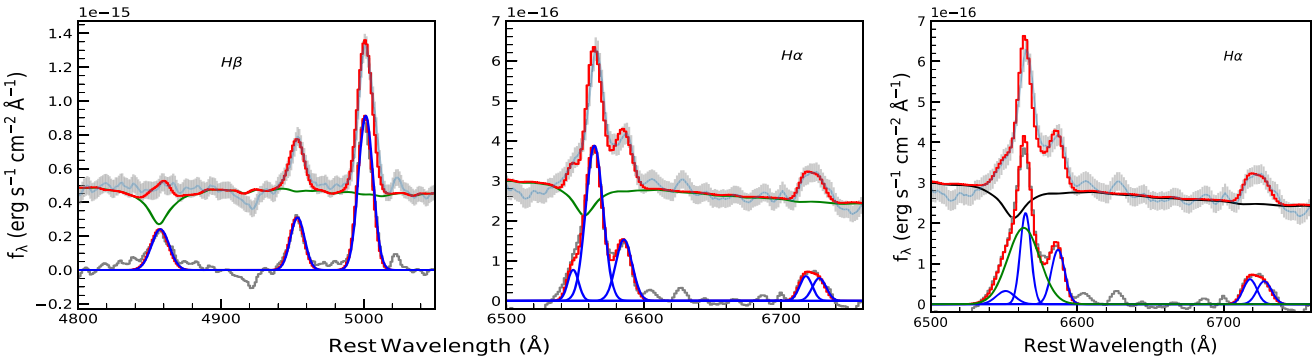

Figure 11. Emission-line fitting of the optical spectrum obtained by HCT. The plot shows the observed data (the solid line with the flux error in gray), the best-fit total model (red), the stellar contribution (green), and the host-subtracted spectrum (gray), with individual narrow lines (Gaussian). There are no broad components in Hβ and Hα in the left and middle panels, respectively, but there is one broad (green—Gaussian) component in Hα in the right panel. The spectrum was smoothened by a 5 pixel box car for visualization purposes only.

line). We note that the preflare state (the pink diamond) was close to that of the expected slope, and possibly the AGN disk–corona emission was related at that time. We also note that when the source went back to the preflare state after the initial flare, the red dots and blue circles were near the expected slope. However, in neither the "initial flare" nor the bright soft state does the disk–corona relation hold.

Similarly, from the right panel of Figure 8, we note that $\alpha_{\rm OX}$ versus $\lambda_{\rm Edd}$ shows no fixed pattern. Ruan et al. (2019) compared the observed correlations between $\alpha_{\rm OX}$ and $\lambda_{\rm Edd}$ in AGNs (including low accretion states $\lambda_{\rm Edd} \sim 10^{-2}$) to those predicted from the observations of X-ray binary outbursts. They found that the observed correlations in AGNs are very similar to the accretion state transitions in typical X-ray binary outbursts, including the inversion of this correlation at $\lambda_{\rm Edd} \sim 10^{-2}$. The right panel of Figure 8 shows that 1ES 1927+654 never went below $\log \lambda_{\rm Edd} < -1.2$, and hence we are confined to only the high accretion phase space of the study by Ruan et al. (2019). The bright soft state is visible (the red squares at the top), but as the UV faded, the X-rays grew in strength, leading to the "high hard" state (the lowest pink square at the bottom right). The red line represents the general AGN behavior, as obtained by Lusso & Risaliti (2016).

4.3. Γ versus λ_{Edd} and Γ versus $L_{2-10\ keV}$ Evolution

In a large sample of ∼7500 AGNs, Sobolewska & Papadakis (2009) found that the average spectral slope Γ does not correlate with source luminosity or BH mass, while it correlates positively with the average $\lambda_{\rm Edd}$. From Figure 3, we find that in the "initial flare," there was no correlation between Γ and $\lambda_{\rm Edd}$ (red data points). However, the bright soft state is different (in blue points). We find that although there has been an increase in the $\lambda_{\rm Edd}$ in this phase, the power-law Γ is very narrowly distributed, around ∼2.5. Similarly, the Γ versus $L_{2-10\ \rm keV}$ plot (Figure 7) shows that the power-law slope is insensitive to the variation in hard X-ray luminosity. The conclusion is that the power-law slope is insensitive to the luminosity and $\lambda_{\rm Edd}$ in the bright soft state.

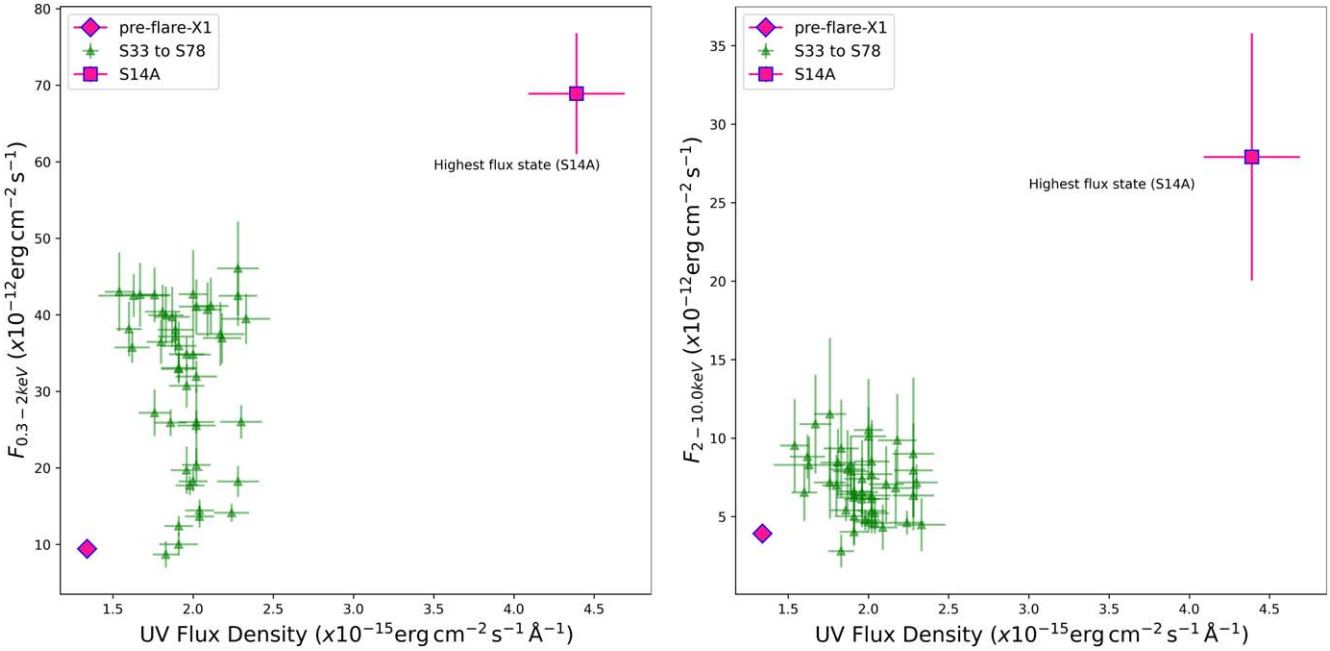

Figure 12. Left: the soft X-ray 0.3–2 keV flux vs. the UVW2 flux density during the bright soft state (i.e., observations S33–S78) exhibits no significant correlation. The bright soft state is plotted in green, the preflare XMM data are plotted in magenta, and the highest flux state is also plotted in magenta. See Table 2 for details. Right: the hard X-ray 2–10 keV flux vs. the UVW2 flux density during the same period as in the left panel similarly shows no statistically significant correlation.

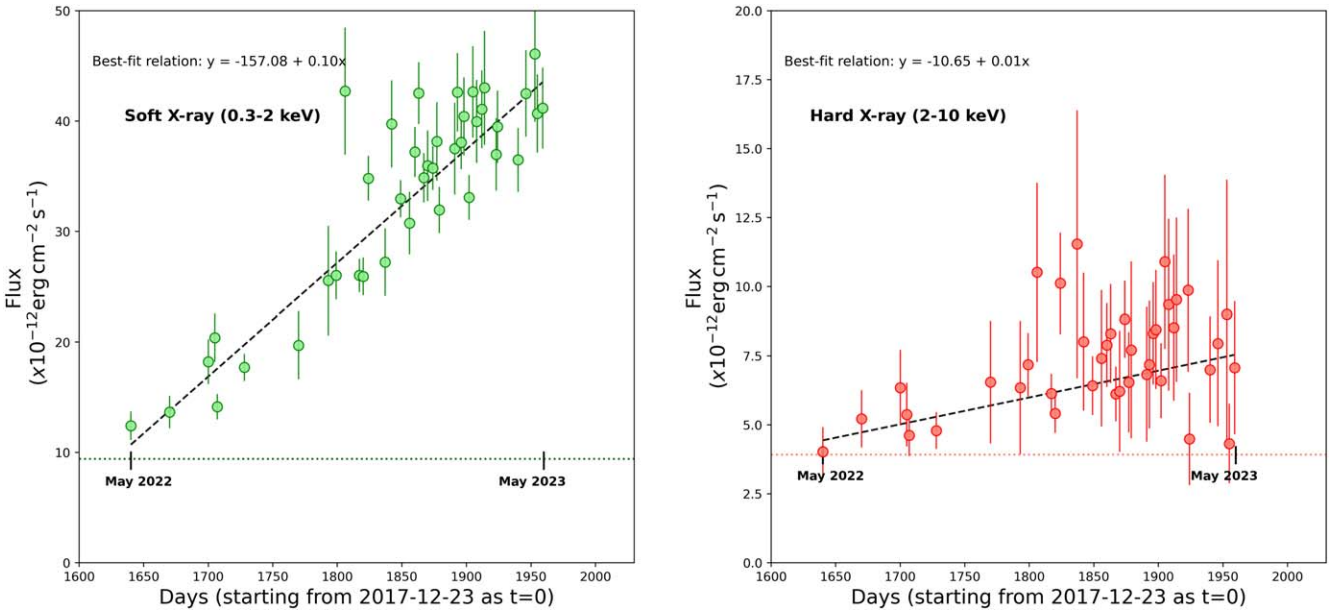

Figure 13. Left: the linear regression fit to the soft X-ray energy increase during the recent bright soft state. Right: the same as the left, but for the hard X-rays. We have estimated the total integrated energy input in the soft and hard X-rays during this time period by integrating under the best-fit line, as shown above. See Section 4.1 for details. The dotted horizontal line represents the preflare flux values obtained from the 2011 XMM-Newton observation.

4.4. The Evolution of the Core and Extended Radio Flux Density

The physical mechanism of the origin of the unresolved core radio emission from radio-quiet AGNs is still unknown (see Panessa et al. 2019; Yang et al. 2020 and references therein). The possible candidates include: (a) the AGN corona (e.g., Yang et al. 2020); (b) low-power jets (e.g., Yao et al. 2021); (c) shocks from winds (e.g., Zakamska & Greene 2014); and (d) rapid star formation (Panessa et al. 2019, 2022; Kawamuro et al. 2022). 1ES 1927+654 has given us a unique glimpse at the core radio emission during and after the violent CL event. From Laha et al. (2022), we note that the core radio emission was at its lowest when the hard X-ray flux was low. Gradually with time, over the next 3 yr (until 2022 March; see also Yang et al. 2022), we found that the radio flux density increased, but never reached its preflare value. In a more recent observation in 2022 August, the core radio flux density decreased, coincidentally when the soft X-ray flux started to rise (the bright soft state). It is, therefore, clear that the core radio flux density is variable over a timescale of months and hence cannot arise out of star formation. It is likely that the core radio emission is related to the corona or the shocks from the winds generated by the violent events, a nascent evolving jet or a low-power jet decreasing in power. Future coordinated X-ray, radio,

and optical–UV monitoring of the source will help us resolve the nature of the radio emission.

The ratio of the unresolved core radio emission at 5 GHz of a radio-quiet AGN to the $L_{2-10\ \mathrm{keV}}$ luminosity follows a unique relation known as the GB relation (see, e.g., Laor & Behar 2008) commonly found in coronally active stars. Table 4 lists the GB relation of the source, and Figure 9 shows the GB light curve. We find that the GB constantly reduced during the violent phase, picked up, and then started to reduce again during the bright soft state, but still within the expected range for radio-quiet AGNs. Further follow-up radio monitoring is currently being undertaken for a better understanding of the radio emission of the source.

4.5. The Optical Spectra

We do not see any significant variations in the emission-line intensity in the optical spectra between the 2021 and 2022 observations, except for the O III emission lines, which have nearly doubled their intensity. We think that the light front from the 2017 December violent event may have just reached the narrowline region. We need further optical monitoring to confirm this scenario.

5. Conclusions

We followed up the enigmatic CL-AGN 1ES 1927+654 with multiwavelength observations spanning a period over 1 yr (2022 January–2023 May). Below we list the most important conclusions.

1. We have observed a recent brightening of the soft X-ray flux since 2022 May, although there is no appreciable change in the UV flux. The total energy pumped into the soft X-rays over a period of 11 months (2022 May 20–2023 May 5) is 3.6×10^{50} erg, and that of the hard X-rays is 5.9×10^{49} erg, an order of magnitude lower. Both the warm Comptonization and the disk reflection scenarios may not be adequate to describe the soft X-rays of this source. The energetics suggest that whatever is producing the SE is pumping out more energy than either the UV or hard X-ray source. This implies that the SE region is either the dominant accreting flow or there is a conduit pumping the accretion energy from the disk to the SE region, rather than radiating it inside the disk.
2. In the bright soft state, we do not detect any correlation between soft X-rays versus UV and hard X-rays versus UV. In addition, we do not see any correlation between: (a) the SE versus the power law; (b) the SE versus UV; and (c) the power law versus UV. The apparent correlation between the soft and hard X-rays is driven by the power law alone, due to the soft nature of the coronal emission ($\Gamma \sim 2.5$–3).
3. The core radio emission (<1 pc) at 5 GHz showed an increase until 2022 March and then a dip in August 2022. It is probably linked to the coronal emission or the shocks from the winds generated by the violent events during the initial flare, a nascent evolving jet, or a low-power jet decreasing in power.
4. The GB relation continuously decreased from the preflare state and is still within the range exhibited by most radio-quiet AGNs.
5. We do not detect any correlations between (a) Γ versus λ_{Edd} and (b) HR versus $L_{2-10\ \mathrm{keV}}$, neither during the "initial flare" nor during the bright soft state. The power-law slope is insensitive to the luminosity and λ_{Edd} in the bright soft state.
6. The data do not follow the α_{OX} versus $L_{2500\ \text{Å}}$ and α_{OX} versus λ_{Edd} relations usually observed in typical AGNs, where the disk–corona synergy is in place.
7. In the optical band, we found that the line intensity of O III has nearly doubled since 2021. We think that the light front from the violent event in 2017 December may have just reached the narrowline region. We need further monitoring of the source to confirm this scenario.

Acknowledgments

We thank the anonymous referee for the insightful comments that helped to better the manuscript. R.G. and S.L. thank Missagh Mehdipour for the helpful discussion. The material is based upon work supported by NASA under award No. 80GSFC21M0002. We acknowledge the use of public data from the Swift data archive and thank the Swift team for approving the Swift DDT request. M.N. is supported by the European Research Council (ERC) under the European Union's Horizon 2020 research and innovation program (grant agreement No. 948381) and by funding from the UK Space Agency. X.L.Y. is supported by the National Science Foundation of China (grant No. 12103076) and the Shanghai Sailing Program (grant No. 21YF1455300). K.E.G. was supported by the Hungarian National Research, Development and Innovation Office (NKFIH), grant No. OTKA K134213.

Data Availability

This research has used new and archival data of the Swift observatory through the High Energy Astrophysics Science Archive Research Center Online Service, provided by the NASA Goddard Space Flight Center. This work has made use of data from VLBA (available in the NRAO Data Archive: https://data.nrao.edu/) and EVN observations (available in the EVN Data Archive at JIVE: http://archive.jive.nl/scripts/portal.php). The National Radio Astronomy Observatory is a facility of the National Science Foundation operated under cooperative agreement by Associated Universities, Inc. EVN is a joint facility of independent European, African, Asian, and North American radio astronomy institutes.

Appendix

The evolution of the X-ray spectra (Figure 14) and the corresponding best-fit model (Figure 15) are shown below to characterize the evolution of 1ES 1927+654 as observed by Swift-XRT.

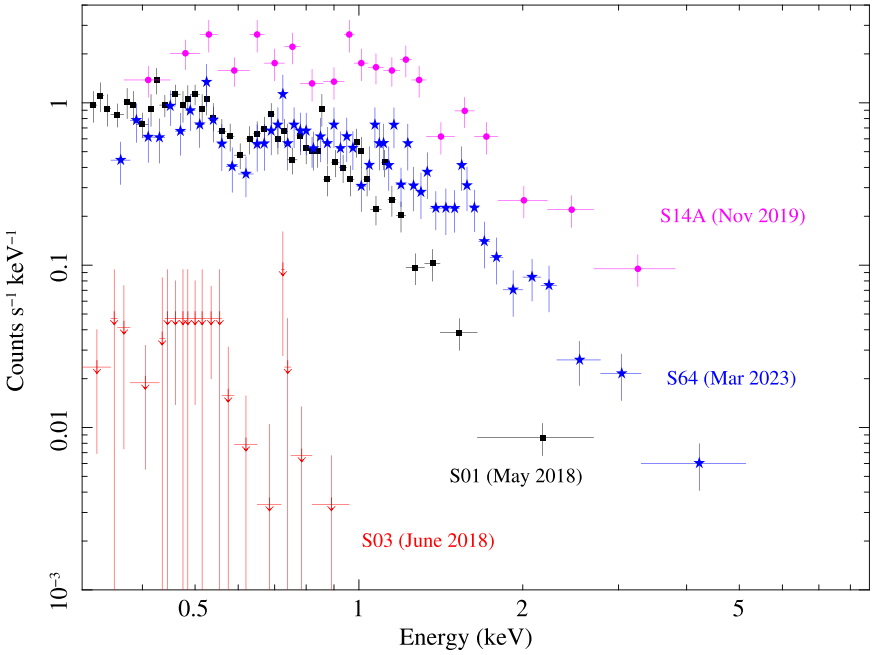

Figure 14. X-ray spectral evolution of 1ES 1927+654 as observed by Swift-XRT. The X-ray spectrum in 2018 May is shown by the black diamond points, when the spectrum was very soft and the spectrum >1 keV was about to vanish (the corona vanished). The lowest flux state (still detectable by XRT) was captured in 2018 June, shown by the red triangular points. The highest flux state (S14A; see Laha et al. 2022) in 2019 November is depicted by the pink circular points. The soft X-ray flux rise in 2023 March (during the bright soft state) is shown by the blue star points. See Table 2 and Laha et al. (2022) for details.

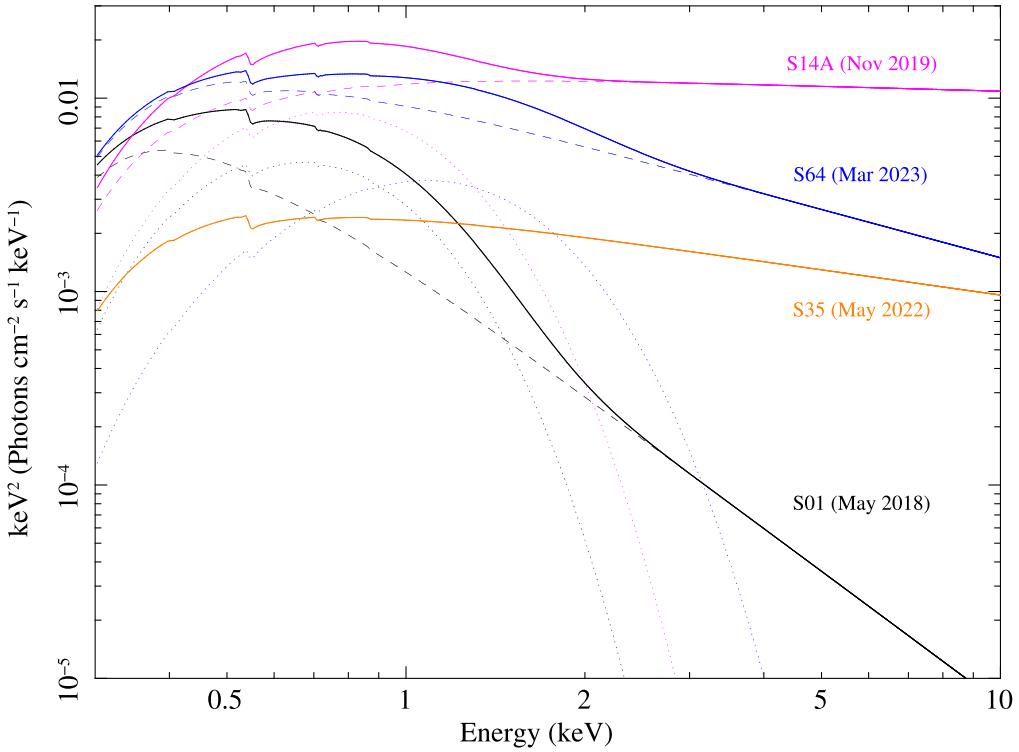

Figure 15. The best-fit model obtained from the spectral fitting of the Swift X-ray observations showing the evolution of 1ES 1927+654. We just included the best-fit models to better visualize the spectral evolution. The dotted, dashed, and solid lines represent the blackbody, power-law, and total spectrum, respectively, for each observation. The model for 2018 May is shown by a black curve featuring a soft spectrum. The highest flux state (S14A; see Laha et al. 2022) in 2019 November is depicted as a magenta curve. S35 represents the recent observation in 2022 May, where the soft and hard X-ray flux returned to the preflare state (as in 2011) and is shown by the orange curve. Here, we did not require any blackbody component to model the spectrum. The soft X-ray flux rise in 2023 March (during the bright soft state, S64) is shown by the blue curve. See Table 2 and Laha et al. (2022) for details.

ORCID iDs

Ritesh Ghosh https://orcid.org/0000-0003-4790-2653
Sibasish Laha https://orcid.org/0000-0003-2714-0487
Agniva Roychowdhury https://orcid.org/0000-0003-1101-8436
Xiaolong Yang https://orcid.org/0000-0002-4439-5580
Suvendu Rakshit https://orcid.org/0000-0002-8377-9667
Ehud Behar https://orcid.org/0000-0001-9735-4873
Francesca Panessa https://orcid.org/0000-0003-0543-3617
Stefano Bianchi https://orcid.org/0000-0002-4622-4240
Fabio La Franca https://orcid.org/0000-0002-1239-2721
Nicolas Scepi https://orcid.org/0000-0002-1239-2721
Mitchell C. Begelman https://orcid.org/0000-0003-0936-8488
Anna Lia Longinotti https://orcid.org/0000-0002-1239-2721
Elisabeta Lusso https://orcid.org/0000-0003-0083-1157
Matt Nicholl https://orcid.org/0000-0002-2555-3192
S. Bradley Cenko https://orcid.org/0000-0003-1673-970X
Brendan O'Connor https://orcid.org/0000-0002-9700-0036
Erica Hammerstein https://orcid.org/0000-0002-5698-8703
Krisztina Éva Gabányi https://orcid.org/0000-0003-1020-1597
Federica Ricci https://orcid.org/0000-0001-5742-5980
Sabyasachi Chattopadhyay https://orcid.org/0000-0003-1601-8048

References

Arnaud, K. A. 1996, in ASP Conf. Ser. 101, Astronomical Data Analysis Software and Systems V, ed. G. H. Jacoby & J. Barnes (San Francisco, CA: ASP), 17
Beasley, A. J., & Conway, J. E. 1995, in ASP Conf. Ser. 82, Very Long Baseline Interferometry and the VLBA, ed. J. A. Zensus, P. J. Diamond, & P. J. Napier (San Francisco, CA: ASP), 327
Bellm, E. C., Kulkarni, S. R., Graham, M. J., et al. 2019, PASP, 131, 018002
Boller, T., Voges, W., Dennefeld, M., et al. 2003, A&A, 397, 557
Briggs, D. S. 1995, AAS Meeting, 187, 112.02
Burrows, D. N., Hill, J. E., Nousek, J. A., et al. 2005, SSRv, 120, 165
Cappellari, M. 2017, MNRAS, 466, 798
Chael, A. A., Johnson, M. D., Bouman, K. L., et al. 2018, ApJ, 857, 23
Denney, K. D., De Rosa, G., Croxall, K., et al. 2014, ApJ, 796, 134
Done, C., Davis, S. W., Jin, C., Blaes, O., & Ward, M. 2012, MNRAS, 420, 1848
Evans, P. A., Beardmore, A. P., Page, K. L., et al. 2009, MNRAS, 397, 1177
Falcón-Barroso, J., Sánchez-Blázquez, P., Vazdekis, A., et al. 2011, A&A, 532, A95
Gallo, L. C., MacMackin, C., Vasudevan, R., et al. 2013, MNRAS, 433, 421
García, J., Dauser, T., Lohfink, A., et al. 2014, ApJ, 782, 76
García, J. A., Kara, E., Walton, D., et al. 2019, ApJ, 871, 88
Gezari, S. 2021, ARA&A, 59, 21
Ghosh, R., Dewangan, G. C., Mallick, L., & Raychaudhuri, B. 2018, MNRAS, 479, 2464
Ghosh, R., Dewangan, G. C., & Raychaudhuri, B. 2016, MNRAS, 456, 554
Ghosh, R., & Laha, S. 2020, MNRAS, 497, 4213
Ghosh, R., & Laha, S. 2021, ApJ, 908, 198
Ghosh, R., Laha, S., Deshmukh, K., et al. 2022, ApJ, 937, 31
Greisen, E. W. 1990, in Seminar on Acquisition, Processing and Archiving of Astronomical Images (Naples: Osservatorio Astronomico di Capodimonte and Centro di Formazione e studi per il Mezzogiorno), 125
Güdel, M., & Benz, A. O. 1993, ApJ, 405, L63
Hinkle, J. T., Kochanek, C. S., Shappee, B. J., et al. 2023, MNRAS, 521, 3517
Kawamuro, T., Ricci, C., Imanishi, M., et al. 2022, ApJ, 938, 87
Kormendy, J., & Ho, L. C. 2013, ARA&A, 51, 511
Kovalev, Y. Y., Kellermann, K. I., Lister, M. L., et al. 2005, aj, 130, 2473
Laha, S., Meyer, E., Roychowdhury, A., et al. 2022, ApJ, 931, 5
LaMassa, S. M., Cales, S., Moran, E. C., et al. 2015, ApJ, 800, 144
Laor, A., & Behar, E. 2008, MNRAS, 390, 847
Li, R., Ho, L. C., Ricci, C., et al. 2022, ApJ, 933, 70
Lusso, E., Comastri, A., Vignali, C., et al. 2010, A&A, 512, A34
Lusso, E., & Risaliti, G. 2016, ApJ, 819, 154
Marconi, A., Risaliti, G., Gilli, R., et al. 2004, MNRAS, 351, 169
Masterson, M., Kara, E., Ricci, C., et al. 2022, ApJ, 934, 35
Mathur, S., Denney, K. D., Gupta, A., et al. 2018, ApJ, 866, 123
McElroy, R. E., Husemann, B., Croom, S. M., et al. 2016, A&A, 593, L8
Mehdipour, M., Branduardi-Raymont, G., Kaastra, J. S., et al. 2011, A&A, 534, A39
Mehdipour, M., Kriss, G. A., Brenneman, L. W., et al. 2022, ApJ, 925, 84
Noda, H., & Done, C. 2018, MNRAS, 480, 3898
Panessa, F., Baldi, R. D., Laor, A., et al. 2019, NatAs, 3, 387
Panessa, F., Pérez-Torres, M., Hernández-García, L., et al. 2022, MNRAS, 510, 718
Parker, M. L., Schartel, N., Grupe, D., et al. 2019, MNRAS, 483, L88
Petrucci, P. O., Gronkiewicz, D., Rozanska, A., et al. 2020, A&A, 634, A85
Petrucci, P. O., Ursini, F., De Rosa, A., et al. 2018, A&A, 611, A59
Prochaska, J., Hennawi, J., Westfall, K., et al. 2020, JOSS, 5, 2308
Rakshit, S., Stalin, C. S., & Kotilainen, J. 2020, ApJS, 249, 17
Ricci, C., Kara, E., Loewenstein, M., et al. 2020, ApJ, 898, L1
Ricci, C., Loewenstein, M., Kara, E., et al. 2021, ApJS, 255, 7
Ricci, C., & Trakhtenbrot, B. 2022, arXiv:2211.05132
Roming, P. W. A., Kennedy, T. E., Mason, K. O., et al. 2005, SSRv, 120, 95
Roychowdhury, A., Meyer, E., & Georganopoulos, M. 2023, submitted
Ruan, J. J., Anderson, S. F., Eracleous, M., et al. 2019, ApJ, 883, 76
Scepi, N., Begelman, M. C., & Dexter, J. 2021, MNRAS, 502, L50
Schawinski, K., Koss, M., Berney, S., & Sartori, L. F. 2015, MNRAS, 451, 2517
Shappee, B. J., Prieto, J. L., Grupe, D., et al. 2014, ApJ, 788, 48
Shepherd, M. C., Pearson, T. J., & Taylor, G. B. 1994, BAAS, 26, 987
Sobolewska, M. A., & Papadakis, I. E. 2009, MNRAS, 399, 1597
Tananbaum, H., Avni, Y., Branduardi, G., et al. 1979, ApJ, 234, L9
Trakhtenbrot, B., Arcavi, I., MacLeod, C. L., et al. 2019, ApJ, 883, 94
Tripathi, P., & Dewangan, G. C. 2022, ApJ, 930, 117
Yang, X., Mohan, P., An, T., et al. 2022, ATel, 15382, 1
Yang, X., Yao, S., Yang, J., et al. 2020, ApJ, 904, 200
Yao, S., Yang, X., Gu, M., et al. 2021, MNRAS, 508, 1305
Zakamska, N. L., & Greene, J. E. 2014, MNRAS, 442, 784